With SI

Journal of The Electrochemical Society, 2022 169 031510 1945-7111/2022/169(3)/031510/13/\$40.00 © 2022 The Electrochemical Society ("EĆS"). Published on behalf of ECS by IOP Publishing Limited





Isothermal Oxidation of $Ti_3Al_{0.6}Ga_{0.4}C_2$ MAX Phase Solid Solution in Air at 1000 °C to 1300 °C

Tarek A. ElMeligy, ¹ Enrica Epifano, ^{2,3} Maxim Sokol, ^{1,4} Gilles Hug, Marcus Hans, Jochen M. Schneider, ⁵ and Michel W. Barsoum ^{1,z}

¹Drexel University, Department of Materials Science & Engineering, Philadelphia, PA, United States of America

²Laboratoire d'Etudes des Microstructures, CNRS-ONERA, Boite Postale 72, 92322 Châtillon Cedex, France

The atomically laminated Ti_2AlC , Ti_3AlC_2 and Cr_2AlC MAX phases, with A=Al, form adherent, passivating α -alumina, Al_2O_3 , oxide scales when heated in air. The effect of solid solutions on the A layers in affecting the oxidation kinetics remains a subject of open research. Herein we synthesize a dense bulk polycrystalline $Ti_3Al_{1-x}Ga_xC_2$ ($x\approx0.4$) solid-solution and investigate its isothermal oxidation in ambient air, in the $1000~^{\circ}C-1300~^{\circ}C$ temperature range, for times varying between 15 and 300 h. At $1000~^{\circ}C$, a passivating dense Al_2O_3 layer ($\approx1-2.6~\mu m$ thick) with near cubic kinetics and an overall weight gain that is slightly less than either Ti_3AlC_2 or Ti_2AlC is formed. At $1200~^{\circ}C$, the Al_2O_3 layer thickens (3.5–12 μm thick) with some scale delamination on the corners initiating at 15 h. At $1300~^{\circ}C$, the Al_2O_3 layer (7.6–20.7 μm thick) wrinkles and Al_2TiO_5 forms. Though the Al_2O_3 grains coarsen at $1200~^{\circ}C$ and $1300~^{\circ}C$, the weight gain is higher than that for Ti_3AlC_2 or Ti_2AlC . At around 7 at. %, this is one of the lowest, if not lowest, Al mole fraction in a Ti-based alloy/compound that forms an Al_2O_3 passivating layer. We further provide compelling microstructural evidence, in the form of a duplex oxide, that at $1000~^{\circ}C$, the outward Al flux, J_{Al} , and the inward O flux, J_{O} , are related such that $2J_{Al}=3J_{O}$. A fraction of these fluxes combine, at the duplex oxide interface, to nucleate small grains © 2022 The Electrochemical Society ("ECS"). Published on behalf of ECS by IOP Publishing Limited. [DOI: 10.1149/1945-7111/ac58c1]

Manuscript submitted October 19, 2021; revised manuscript received January 10, 2022. Published March 23, 2022.

Supplementary material for this article is available online

The lack of materials capable of withstanding extreme environments often imposes the greatest technical barrier to the development and improvements of a wide range of important technologies and applications. ^{1–3} Transportation, aerospace, energy conversion, power generation, and defense technologies, among others, call for novel structural and multifunctional materials that are capable of operating under harsh conditions such as high temperatures, oxidizing and/or corrosive environments, extreme thermal cycles and mechanical loads, etc. ^{4,5} Conditions that are challenging for even the most advanced high-temperature metallic alloys. Various aluminum-containing alloys (e.g. FeCrAl-based, NiCrAl-based, Ti_xAl_y, among others) are oxidation-resistant at high temperatures, HTs, because they form adherent α-alumina, Al₂O₃ layers.

A class of thermodynamically stable machinable, nanolayered ternary carbides and nitrides, known as the MAX phases, has attracted considerable attention since they possess properties that combine some of the best qualities of ceramics and metals.⁶⁻⁹ MAX phases are a family of more than 150 compounds having a general chemical formula $M_{n+1}AX_n$, where n is 1, 2, 3 or 4, M is an early transition metal (Ti, Cr, Zr, Mo, Ta, etc.), A is an A-group element mostly from groups 13-16 (Al, Si, Ge, As, In, etc.) and X is C, N or B. 8,9 What renders some of the MAX phases especially attractive for applications in oxidizing environments is that they form adherent, tenacious and self-healing Al₂O₃ layers. Those layers are resistant to thermal shock, thermal cycling, and corrosive environments.¹³ Moreover, some of the MAX phases are not only light, stiff and refractory like typical ceramics, but also damage tolerant, pseudo-ductile at high temperatures, and readily machinable which bodes well for their use in HT applications.

Of all the MAX phases characterized to date, ^{12–26} Ti₃AlC₂, Ti₂AlC, and Cr₂AlC offer the best resistance in oxidizing environments at HT, thanks to the formation of highly stable and dense Al₂O₃ layers, with some of the slowest growth kinetics measured in any passive oxide layer forming materials. ⁸ In fact, comparison with state-of-the-art Al₂O₃ forming austenitic stainless steels (AFAS)^{13,20}

suggests that the oxidation behavior in all high-performing Al_2O_3 -forming systems is ultimately controlled by the same underlying mechanism, namely, O and/or Al diffusion through α -Al₂O₃ grain boundaries, GBs. Essentially, both AFAS and Al_2O_3 -forming MAX compounds act as Al reservoirs that enable fast diffusion of Al towards the reservoir/Al₂O₃ interface, where it reacts with oxygen to form the protective Al_2O_3 layer.

Smialek's work²⁰ further elucidates the rate-controlling mechanism of GB diffusion across the growing Al₂O₃ grains leading to cubic oxidation kinetics across various Al₂O₃ forming alloys and compounds. It is also important to note that Al₂O₃ has a coefficient of thermal expansion (CTE) close to that of Ti₂AlC. As a result, the stresses thermally induced in the scales are relatively low²⁷ compared to other MAX phases making them resistant to spallation even after 10,000 thermal cycles to 1350 °C.²⁸

Several research groups have focused on developing Al-based MAX solid solutions. For example, $Ti_3(Al_{1-x}Si_x)C_2$, $^{29-31}$ $Ti_3Al_xSn_{1-x}C_2$ 32,33 and $Ti_2Al(C_{1-x}N_x)^{34,35}$ show improved mechanical properties due to a solid solution hardening effect. Others, such as $Cr_2(Al_{1-x}Si_x)C$, 36 ($Ti_1Nb)_2AlC^{37,38}$ exhibit solid solution softening. The reasons for these observations remain a subject of study, but clearly show that it is possible to tune MAX phase properties by solid solution alloying on the A-layers.

The challenge is to enhance the mechanical properties most importantly, creep resistance without sacrificing the oxidation resistance. Gao et al. showed that the compressive strength of $\rm Ti_3(Al_{1-x}Si_x)C_2$ solid solutions can be improved by more than 30% compared to their end members, 29 notably without sacrificing their oxidation resistance. However, looking for optimal Al-MAX solid solutions that could potentially provide both improved mechanical properties in general, and creep properties in particular, as well as, maintaining their excellent oxidation resistance remains uncharted territory.

Herein, we chose to alloy Ga on the Al-layers hoping that a mixed Ga_2O_3 and Al_2O_3 oxide would form that would have even better oxidation resistance than Al_2O_3 alone. Ga_2O_3 and Al_2O_3 oxide form a complete solid solution over the entire composition range. ³⁹ To that effect, we successfully synthesized a fully dense, bulk

³CIRIMAT laboratory, University of Toulouse, CNRS, INPT, UPS, ENSIACET 4 allée Emile Monso, BP-44362, 31030 Toulouse Cedex 4, France

⁴Department of Materials Science and Engineering, Tel Aviv University, Ramat Aviv 6997801, Israel

⁵Materials Chemistry, RWTH Aachen University, Aachen, Germany

 $Ti_3Al_{1-x}Ga_xC_2$ solid-solution with $x\approx 0.4$ and studied its isothermal oxidation in ambient air, in the 1000 °C-1300 °C temperature range, for times as long as 300 h. Although we did not obtain a mixed oxide, we did form an Al_2O_3 scale despite the fact that the Al atomic content was only 10%.

Experimental

Synthesis.—To synthesize Ti_3AlC_2 , Ti, TiC and Al reagents were mixed in molar ratios listed in Table I. The powders were mixed in a polyethylene jar with zirconia milling balls for ~ 9 h. The mixed powders were inserted, and hand compacted in a 38.1 mm diameter graphite die coated with boron nitride, BN, release spray and layered with graphite foil. The powder mix was reactively hotpressed (HPed) under a load corresponding to a pressure of ~ 12 MPa, applied 15 min after reaching the dwell temperature. The heating rate was 400 °C h⁻¹, with a dwell time of 5 h at 1500 °C. After furnace cooling, the sample's surfaces were ground using coarse diamond pads (120 grit) to remove residual graphite foil bonded to its surface. The sample was then milled using a TiN-coated end mill bit to obtain Ti_3AlC_2 powder.

To synthesize Ti_3GaC_2 , Ti, TiC, and Ga reagents listed in Table I were mixed in tabulated molar ratios. In this case, Ga, in the form of a solid rod, was placed in a polyethylene jar together with the other powders. The jar was heated to 50 °C for 0.5 h until Ga melted and wetted the other reactant powders. After cooling to room temperature, RT, the mixture was ball mixed for \sim 9 h. The powders were then reactively hot-pressed at a rate of 400 °C h⁻¹, up to 1400 °C, and held at that temperature for 3 h at a stress of 12 MPa applied 15 m after reaching the dwell temperature. The HPed samples were then drilled to obtain Ti_3GaC_2 powders.

To fabricate the solid solution, the Ti_3AlC_2 and Ti_3GaC_2 powders were sieved to -325 mesh size, mixed in 3:2 molar ratio and ball milled for ~ 9 h. The mixture was HPed at 1500 °C for 5 h at 400 °C h⁻¹ and a load corresponding to a stress of ~ 22 MPa.

The HPed $\rm Ti_3Al_{0.6}Ga_{0.4}C_2$ sample of 38.3 mm diameter and 2.5 mm thickness was ground with coarse diamond pads to remove residual graphite bonded to the surface. The sample was then progressively ground and polished using SiC paper in the 400–1200 grit range and cleaned with ethanol and dried.

Oxidation testing.—Bulk samples were electrically discharge machined (EDMed) into rectangular slabs ($5.8 \times 5.8 \times 2.3 \text{ mm}^3$). Prior to characterization, the samples were re-polished with 1200 grit SiC paper and finally down to 3 μ m with a diamond suspension. This step is important to remove any residue from the EDM step that can interfere with the formation of the Al₂O₃ layer.

A Textured $\rm Ti_2AlC$ rectangular slab $(6.4 \times 4.8 \times 1.8 \ mm^3)$, used for grain size comparison, was machined out of a bulk sample with a diamond-coated saw and polished using SiC paper in the 400-1200 grit range then cleaned with ethanol and dried. The synthesis procedure for the textured $\rm Ti_2AlC$ is mentioned elsewhere. 40

The samples were first weighed before placing them in Al_2O_3 crucibles that were in turn placed in a box furnace and heated under static, ambient air. Experiments were performed at $1000\,^{\circ}\text{C}$, $1200\,^{\circ}\text{C}$, and $1300\,^{\circ}\text{C}$. The samples were placed inside the furnace near the center of the hot zone and heated at $4\,^{\circ}\text{C}$ min⁻¹ up to the target oxidation temperature. Samples were periodically taken out at each oxidation temperature. The oxidized samples were visually inspected, weighed, and checked for macroscopic changes in their dimensions.

Characterization.—XRD was performed using a powder diffractometer (SmartLab, Rigaku Corp., Tokyo, Japan) with Cu-Kα radiation in Bragg Brentano scan mode. Drilled powder XRD patterns of Ti₃AlC₂, Ti₃GaC₂ precursors, and the Ti₃Al_{0.6}Ga_{0.4}C₂ solid solution were obtained before oxidation. The powder samples were scanned in the $2\theta = 5-150^\circ$ range, with a step size of 0.02° and a dwell time of 4.5 s per step. Lattice parameters of the end members

and the reactively HPed solid solution $Ti_3Al_{0.6}Ga_{0.4}C_2$ powders were determined from Rietveld analysis of the XRD patterns, using the Fullprof Suite. ⁴¹ Statistical uncertainties in all subsequent measurements are included in parentheses after each value. The Rietveld refinements were all performed using the crystal structure of Ti_3AlC_2 , (P63/mmc space group), where Ti atoms occupy the 2a and 4f Wyckoff positions, Al atoms are in 2b positions and C atoms are in 4f positions. Lattice parameters and atomic positions were all refined during the analysis. A Pseudo-Voigt function was adopted for the peak shape profile. The XRD patterns were satisfactorily refined, with goodness parameters $R_p < 13$ and $R_{wp} < 12$.

XRD patterns were acquired from the oxidized surfaces in the 5° – 100° 2θ range with a step size of 0.02° and dwell time of 0.6 s per step. Phase identification of the oxide phases formed on the surface was performed by profile matching of XRD patterns.

Micrographs and relative elemental compositions, phase analysis, and elemental maps were obtained using a scanning electron microscope, SEM (Zeiss Supra 50 VP, Carl Zeiss SMT AG, Oberkochen, Germany), equipped with an energy-dispersive X-ray spectroscope, EDS, (Oxford EDS, Oxfordshire, United Kingdom). The reported EDS values represent a combination of spot and area scans selected from various regions on samples polished to 1 μ m. An accelerating voltage of 20 kV and 15–60 s dwell times were used for the EDS measurement at a 15 mm working distance (WD) and a 60 μ m aperture size.

The oxidized samples were also examined in an SEM to view their surface oxide morphologies. Fractured oxidized samples were cold-mounted in epoxy and ground first using 240–1200 SiC grit paper and then down to 1 μ m with diamond suspension. Oxide-scale thicknesses were measured from the SEM micrographs using ImageJ software with each data point being the arithmetic mean of 1024 equally spaced measurements along the scale length with the aid of a slicing addon. The oxide scale grain sizes were estimated from both oxidized sample surfaces and fracture surface micrographs by taking the average measurement of 5–40 grains across the oxide thickness.

In addition, the microstructure of the sample oxidized at 1000 °C for 300 h was characterized by scanning transmission electron microscopy (STEM). A cross-sectional thin lamella was prepared by focused ion beam (FIB) techniques in a dual-beam microscope (Helios Nanolab 660, FEI, Hillsboro, OR, USA) and Ga ions were used at an acceleration voltage of 30 kV. First, the region of interest from the oxidized sample surface was protected with a 2 μ m thick Pt layer. After trench milling, the lamella was extracted with an EasyLift manipulation needle and placed on a Cu omniprobe. Sequential thinning of the lamella to a final thickness of approximately 80 nm was done using currents of 0.79, 0.43, 0.23, and 0.08 μ A. Bright-field images were acquired using a STEM III detector at 30 kV acceleration voltage. EDS line profiles with a step size of 50 nm were performed at 10 kV acceleration voltage using an Octane Elect detector.

Local chemical composition analysis of the interface between oxide scale and MAX phase (1000 °C, 300 h) was carried out by three-dimensional atom probe tomography (APT). The local electrode atom probe (LEAP 4000X HR, Cameca, Madison, WI, USA) was equipped with a reflectron and the flight path length was 382 mm. Field evaporation was employed by thermal pulsing with a UV laser at 50 pJ energy and 125 kHz frequency. The base temperature was 60 K, the detection rate was set at 5 ions out of 1000 pulses and 7 million ions were collected. IVAS 3.8.6 was used for the reconstruction of atomic positions and data analysis. Needleshape atom probe specimens were prepared by FIB according to a standard protocol and the oxide scale was removed close to the oxide-MAX phase interface at 5 kV and 40 pA in order to reduce the contamination from Ga ions used for specimen preparation $^{\rm 42}$

Results

Solid-solution phase structure and composition.—Rietveld refinement of XRD patterns was used to estimate phase composition as

Phase	Reagent	Molar ratio	Supplier	Purity (metal basis)	Particle Size (μm)	Temp. (°C)	Pressure (MPa)	Dwell time (h)
Ti ₃ AlC ₂	Ti	1	Alfa Aesar	99.5%	≤ 44 (-325 mesh)	1500	12	5
	TiC	2	H.C. Starck	98%	Between 5.6 and 22.5			
	Al	1.05	Alfa Aesar	99.5	≤ 44 (-325 mesh)			
Ti_3GaC_2	Ti	1	Alfa Aesar	99.5%	≤ 44 (-325 mesh)	1400		3
	TiC	2	H.C. Starck	98%	Between 5.6 and 22.5			
	Ga	1.15	Gallant	99.99%	Rod			
			Metals					
SS		$Ti_3Al_{0.6}Ga_{0.4}C_2$				1500	22	5

well as lattice parameters, LPs (Fig. S2 (available online at stacks. iop.org/JES/169/031510/mmedia)). The fitting was based on a hexagonal crystal structure (space group P 6₃/mmc), with refined lattice parameters of a = b = 3.083 Å and c = 18.455 Å. EDS spot and area analysis of bulk Ti₃Al_{0.6}Ga_{0.4}C₂ cross-sections (not shown). shows a Ga:(Ga+Al) ratio of (0.37 \pm 0.03):1 which implies x \approx 0.4. The fracture surface in Figs. S3a–S3b demonstrates the typical nano-laminated MAX structure with an average grain size of 35 \pm 10 μm .

Isothermal Oxidation kinetics and activation energies.—The time, t, dependence of the mass gain per unit area, $\Delta W/A$, obtained at 1000 °C, 1200 °C, and 1300 °C is shown in Fig. 1a. Each data point represents a different sample. At 1000 °C, the mass increase is initially rapid with time before slowing down. At this temperature, initially the mass gain for the Ti₃Al_{0.6}Ga_{0.4}C₂ sample is 15% less than that reported for either Ti₂AlC or Ti₃AlC₂. ^{44–46} After 300 h, the Ti₃Al_{0.6}Ga_{0.4}C₂ weight gain is about 20% lower than that of Ti₂AlC and 14% lower than that reported for Ti₃AlC₂. ⁴⁵

After 300 h of oxidation at 1200 °C, the weight gain for the solid solution is greater than that of Ti_2AIC and Ti_3AIC_2 by $\approx 57\%$ and $\approx 45\%$, respectively (Fig. 1a).

At 1300 °C the weight gain after 240 h of oxidation for our solid solution is more than double that of Ti_2AlC and Ti_3AlC_2 . At 1300 °C, the Al_2TiO_5 phase also forms through a reaction between TiO_2 and Al_2O_3 . Given this poor oxidation resistance, the results at this temperature will only be discussed in a cursory manner.

The Δ W/A results were analyzed assuming cubic, parabolic and power-law kinetics, assuming the following relationships were operative, respectively:

$$\left(\frac{\Delta W}{A}\right)^3 = k_{c,w}t$$
 [1]

$$\left(\frac{\Delta W}{A}\right)^2 = k_{p,w}t \tag{2}$$

$$\frac{\Delta W}{A} = k't^n \tag{3}$$

where $k_{c,w}$, $k_{p,w}$ and k' are the cubic, parabolic, and power-law constants, respectively; n is the power-law exponent. The estimated rate constants, rate exponents n and corresponding correlation

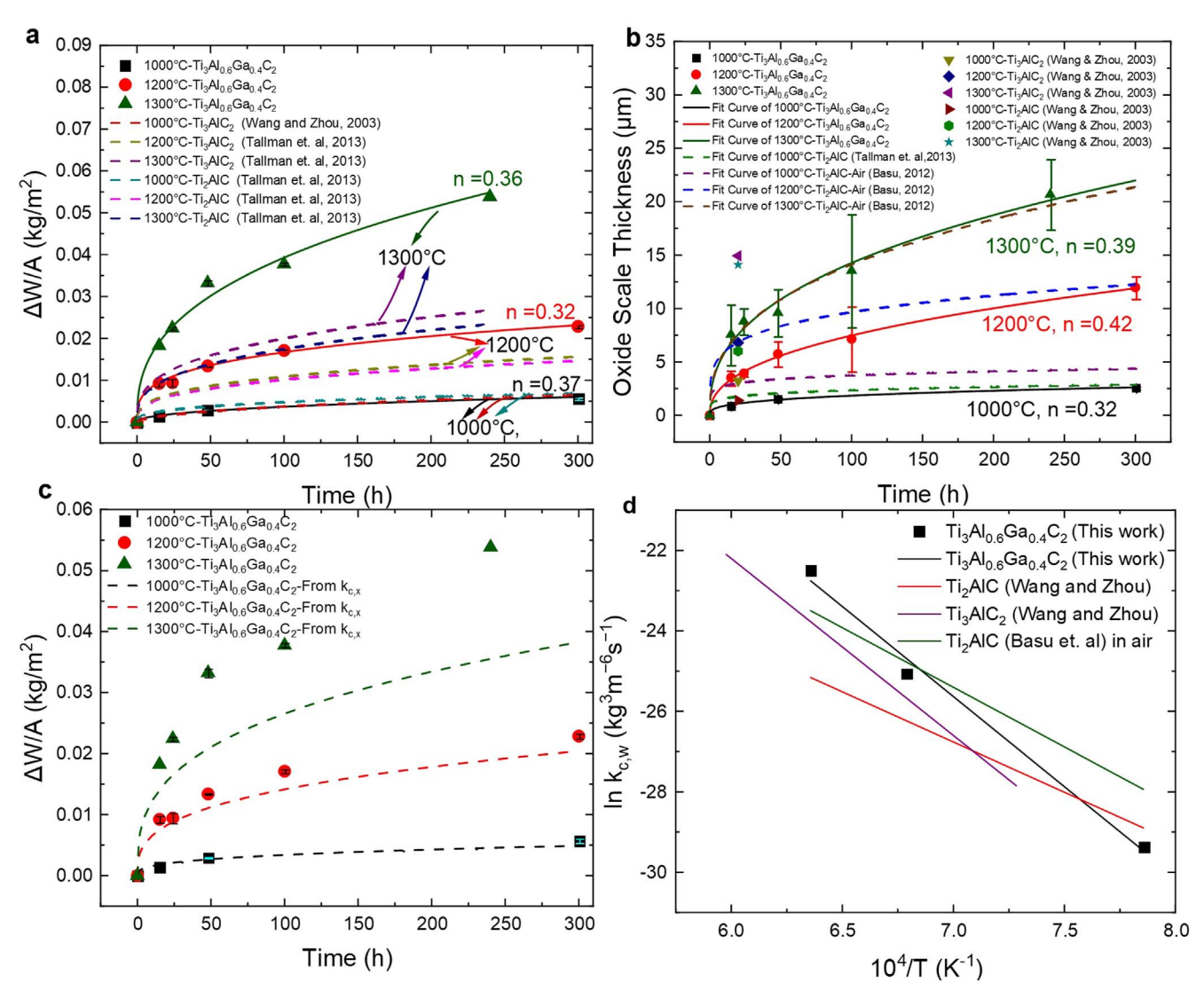


Figure 1. (a) Temperature dependence of weight gain per unit surface area, and (b) scale thickness, as a function of time for $Ti_3Al_{0.6}Ga_{0.4}C_2$. Note that $1 \text{ kg/m}^2 = 10^2 \text{ mg/cm}^2$. Thicknesses and error bars in (b) represent the mean of 1024 automatic scale thickness measurements across polished mounted cross-section samples. Markers represent experimental points. Dashed lines represent power-law fits of kinetics. (c) Weight gains predicted from scale thickness distinction in Table III, compared to experimental weight gain measurements. (d) Arrhenian plot for cubic rate constant $k_{c,w}$. Other results are taken from Refs. 24, 45, 47

coefficients, R², are summarized in Table II. An alternative method for estimation of parabolic weight gain rate constants was formulated by Pieraggi⁴⁸ by using the slope of the weight gain with the square root of time. These rate constants are summarized in Table S1 and Fig. S1. The results are within the same order of magnitude as the rate constants obtained from weight gain versus time curves.

The temperature and time dependencies of the oxide thickness, x, are plotted in Fig. 1b. A summary of the fits -where the k_p values in Eqs. 1 to 3 are replaced by k_x , and $\Delta W/A$ is replaced by x - are shown in Table III. The weight gain and scale thickening results reveal that:

- i. At all temperatures in Table II, the highest R^2 values are for the cubic fits for weight gain. Henceforth when discussing the weight gain kinetics, cubic kinetics, viz. n=3, will be assumed.
- ii. At 1200 °C scale thickening is sub-parabolic (n = 0.42), while weight gain kinetics are closer to cubic (n = 0.32).

As a check for the correctness of the kinetics fit assumed, the $k_{c,x}$ values in Table III were converted to $k_{c,w}$ by assuming the formation of fully dense α -Al₂O₃ with a density of 3950 kg m⁻³. $k_{c,x}$ values were multiplied by (3950 kg m⁻³ × 0.47)³ = (6.4 × 10⁹), where 0.47 is the mass fraction of O in α -Al₂O₃. Figure 1c compares both actual measured weight gain with predicted weight gain based on cubic scale thickening kinetics converted to weight gain. At 1000 °C the agreement is excellent. At 1200 °C, the experimental points are higher than those predicted on oxide thickness alone. At 1300 °C the discrepancy is even higher.

The fitted cubic rate constants may be correlated to temperature through an Arrhenius-type equation:

$$k_{c,w} = k_0 \exp\left(-\frac{Q}{RT}\right)$$
 [4]

where k_0 is the pre-exponential factor, R is the universal gas constant and T is the absolute temperature while Q is the apparent or effective activation energy representing the rate-controlling step of the operative diffusion mechanism. Figure 1d plots the best-fit line of weight gain rate constant as a function of reciprocal temperature, the slope of the linear fit based on cubic kinetics yields an apparent activation $Q_{app}=191~kJ~mol^{-1}$. $1300~^{\circ}C$ data point is excluded from activation energy calculation due to the formation of Al_2TiO_5 at that temperature.

XRD on oxidized samples.—XRD patterns before and after oxidation are shown in Figs. 2–4, at 1000 °C, 1200 °C, and 1300 °C, respectively, as a function of time. For all three cases, the appearance of additional peaks is observed in the oxidized samples, as expected. Moreover, a small shift of the Ti₃Al_{0.6}Ga_{0.4}C₂ reflections toward higher angles was systematically observed.

At 1000 °C, the MAX peaks in the oxidized sample remain the most intense, even after 300 h of oxidation, implying the scale must be quite thin. Next to the substrate peaks, $\alpha\text{-Al}_2O_3$ peaks are clearly observed in all oxidized samples, at all times. A very low-intensity peak around 27.46 °- that coincides with the most intense (110) reflection in TiO $_2$ - was observed after 100 h.

After oxidation at 1200 °C, for 24 h, the intensities of the Al_2O_3 peaks are higher than those of the MAX phase.

After oxidation at 1300 °C, the Al₂O₃ peak intensities dominate at times as low as 48 h. TiO₂ peaks are visible after 15 h of oxidation. The intensity of these peaks is still quite low in comparison to the other observed phases, but higher than those observed at the lower temperatures. At 1300 °C, an additional phase (marked as * in Fig. 4) can be observed from 48 h onward, corresponding to Al₂TiO₅. No pure Ga-oxide peaks were observed in any of the oxidized samples.

Scale morphologies, phase compositions, and grain growth.— Figure 5 shows surface and cross-sectional-fractured and polished - SEM micrographs of most of the samples tested herein. At 1000 °C, Figs. 5d, 5g show the presence of a dense adherent Al₂O₃ scale, with a grain size <1 μ m (~0.1–0.5 μ m). After 300 h, the Al₂O₃ layer is thicker but still adherent (Figs. 5m, 5p). At 1200 °C, the Al₂O₃ layer is dense (Figs. 5e, 5h, 5n, 5q) with larger grains (~1.67–4.05 μ m) than at 1000 °C (Figs. 5b, 5k).

At 1300 °C, localized thick TiO₂ regions form on top of the Al₂O₃ after 15 h (Fig. 5i), and the Al₂O₃ layers wrinkle (Fig. 5r). Cracks are observed to propagate through TiO₂ and Al₂TiO₅ (Fig. 5i).

Surface EDS map after oxidation at 1000 °C for 15 h (Fig. 6a) shows a dense α -Al₂O₃ surface with sparse TiO₂ islands. Polished cross-section (Fig. 6b) indicates trace amounts of Ti and Ga in the vicinity of the Al₂O₃ layer which is most likely originating from the MAX phase. Al-rich intermetallic impurities with Ti:Al:Ga molar ratio of 1.00:1.60 \pm 0.2:0.21 \pm 0.01 are identified along the MAX GBs (Fig. 6b). At 300 h, the surface morphology shows imprinted ridges in the oxide along the substrate GBs (Fig. 6c). Al₂O₃ extends through surface cracks (Fig. 6d) to form sub-surface Al₂O₃, this phenomenon may lead to susceptibility to thermal cycling. After 300 h, the Al₂O₃ layer thickens (Figs. 6b, 6d). Interestingly if the TiO₂ islands coarsened (Figs. 6a, 6c) it is not very noticeable. Their density increases slightly. No TiC regions are detected.

After oxidation at 1200 °C EDS maps (Fig. S4) show no qualitative differences in the surface morphologies and cross-sectional SEM micrographs of the scale. Here again, TiO₂ particles appear on the surface of a dense, adherent Al₂O₃ layer (Figs. S4a–S4h). Not surprisingly, the grain sizes of both phases coarsen. Pores (Fig. S4g) are observed between the TiO₂ and Al₂O₃ phases.

After oxidation at 1300 °C for 15 h EDS maps (Figs. S5a–S5d) shows the formation of ternary Al_2TiO_5 with visible cracks and erosion (Figs. S5c–S5d) at the GBs underneath creating favorable paths for diffusion. Further investigation of the scale surface after 100 h (Fig. S5e–S5f) indicates the presence of coarse TiO_2 . Wrinkled Al_2O_3 with large cavities at the interface (Fig. S5g) are filled with intermetallic impurity of Ti:Al:Ga with molar ratio of $1:2.35 \pm 0.05:0.43 \pm 0.01$ (Fig. S5g).

After 240 h of oxidation at 1300 °C, Al_2TiO_5 (Figs. S5i–S5j) reveals Ga traces (0.15(6) at%) with O:Al:Ti:Ga atomic ratio of 5.5 \pm 0.5:1.4 \pm 0.3:1:0.2 \pm 0.1 and cavities underneath (Figs. S5i–S5j).

EDS line profiles through Al_2O_3 (Figs. S6–7) show a relative increase in the concentration of Al and O content concomitant with a relative decrease in Ti signal as the scan transitions from TiO_2 to Al_2TiO_5 region. Sample corners at 1000 °C (Fig. 7) demonstrate

Table II. Weight gain kinetic parameters and correlation coefficients derived by fitting oxidation experimental results (Fig. 1a).

	Cubic		Parabolic		Power Law		
T (°C)	$k_{c,w} (kg^3m^{-6}s^{-1})$	R ²	$k_{p,w} (kg^2m^{-4}s^{-1})$	R ²	k' (kgm ⁻² s ⁻¹)	n	R ²
1300	$1.6 \pm 0.1 \times 10^{-10}$	0.9736	$4.5 \pm 0.4 \times 10^{-9}$	0.9521	$4 \pm 2 \times 10^{-4}$	0.36 ± 0.04	0.9370
1200	$1.1 \pm 0.1 \times 10^{-11}$	0.9903	$5.3 \pm 0.4 \times 10^{-10}$	0.9372	$2.5 \pm 0.5 \times 10^{-4}$	0.32 ± 0.02	0.9796
1000	$1.45 \pm 0.03 \times 10^{-13}$	0.9986	$2.8 \pm 0.3 \times 10^{-11}$	0.9660	$3 \pm 2 \times 10^{-5}$	0.37 ± 0.05	0.9712

Table III. Scale thickness kinetic parameters and correlation coefficients derived by fitting experimental results (Fig. 1b).

	Cubic		Parabolic		Power Law		
T (°C)	$k_{c,x} (m^3 s^{-1})$	\mathbb{R}^2	$k_{p,x} (m^2 s^{-1})$	R^2	k' (ms ⁻¹)	n	\mathbb{R}^2
1300	$8 \pm 1 \times 10^{-21}$	0.9766	$5.4 \pm 0.5 \times 10^{-16}$	0.9592	$10 \pm 5 \times 10^{-8}$	0.39 ± 0.04	0.9730
1200	$1.2 \pm 0.2 \times 10^{-21}$	0.9732	$1.5 \pm 0.5 \times 10^{-16}$	0.9814	$3.5 \pm 0.5 \times 10^{-8}$	0.42 ± 0.02	0.9948
1000	$1.7 \pm 0.1 \times 10^{-23}$	0.9933	$8 \pm 2 \times 10^{-18}$	0.9127	$3 \pm 2 \times 10^{-8}$	0.32 ± 0.04	0.9847

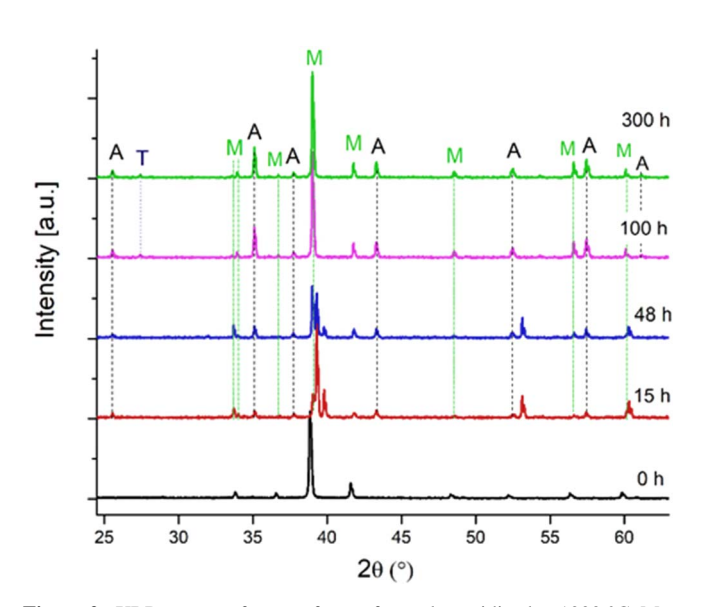


Figure 2. XRD patterns from surfaces of samples oxidized at 1000 °C. M = MAX phase Ti_3AlC_2 -type, $A = Al_2O_3$, $T = TiO_2$.

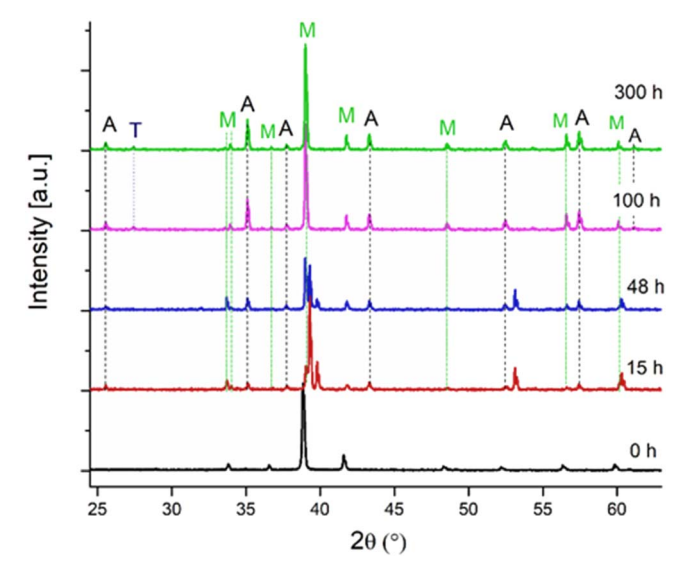


Figure 3. XRD patterns from surfaces of samples oxidized at 1200 °C. M = MAX phase Ti_3AlC_2 -type, $A = Al_2O_3$, $T = TiO_2$.

adherent Al_2O_3 with deviation from corner perpendicularity. At $1200~^{\circ}C$ (Figs. S8a, S8b) the corners are distorted and $1300~^{\circ}C$ (Figs. S8e, S8d) Al_2O_3 distorts into wrinkles and is extruded away from the substrate

The Al_2O_3 grains near the substrate are larger than those closer to the surface (Fig. S8d). This variation in grain size across the scale has been observed by Golightly, F. A. et al.⁴⁹ and later by Naumenko et al.⁵⁰ in FeCrAl(Y) alloys, as well as by Kota et al.⁵¹ for

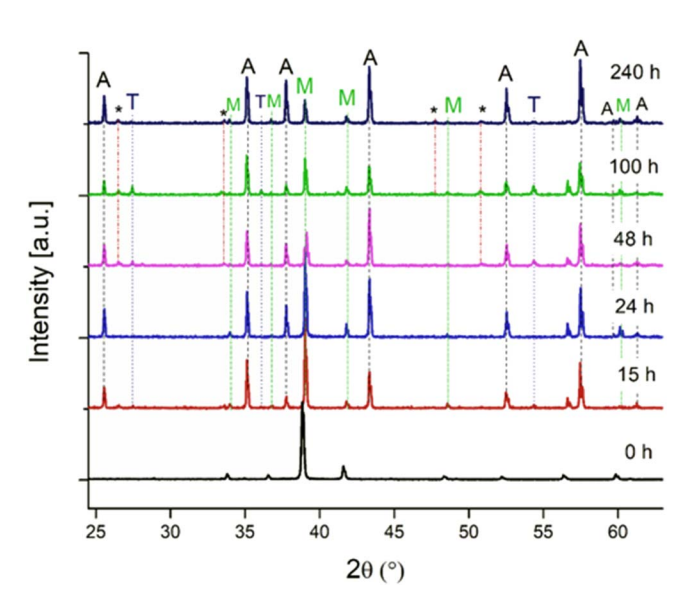


Figure 4. XRD patterns acquired on the samples after iso-thermal oxidation at 1300 °C. M = MAX phase Ti_3AlC_2 -type, A = Al_2O_3 , T = TiO_2 , * = Al_2TiO_5 .

Al₂O₃-forming MoAlB. Grain growth with oxidation time (Fig. 8a) shows that grain size (\sim 0.5–0.8 μ m) at 1000 °C (see Fig. 8a) after 300 h is in agreement with textured Ti₂AlC (see Ref. 40 for synthesis details).

Conversely, the addition of Ga in $Ti_3Al_{0.6}Ga_{0.4}C_2$ results in Al_2O_3 grain sizes at 1200 °C (\sim 1.2–3.7 μm) (Fig. 8a) that are *larger* than those that form on Ti_2AlC .

Oxygen GB diffusivity (Fig. 8b) for Al-forming MAX and MAB phases follow a similar trend on a FeCrAl alloy reference line. Grain growth kinetics as a function of temperature (Fig. 8c) shows the grain size growth for $Ti_3Al_{0.6}Ga_{0.4}C_2$ to be comparable to that of FeCrAl(Zr) alloy studied by Smialek et al. 54 The activation energy for grain growth for $Ti_3Al_{0.6}Ga_{0.4}C_2$ is estimated to be $\approx\!281~\text{kJ}~\text{mol}^{-1}$.

High-resolution grain imaging and Ga allocation.—High-resolution STEM imaging (Fig. 9a) at 1000 °C after 300 h of oxidation shows a multi oxide layer of an outer equiaxed grain region (0.9 μ m thick), an inner columnar grain region (1.4 μ m thick) in contact with the substrate, and interface region (0.4 μ m thick). Crucially no Ga is detected in the oxide but only in the MAX phase (Fig. 9a). Ga in the Pt protection layer is from the lamella preparation process and any elemental gradients are attributed to EDX resolution limitations.

ATP of a columnar grain above the substrate (Fig. 9b) shows the elemental distribution across the oxide-MAX interface. Mass spectrum data shows no Ti, C, nor Ga within the oxide grain which is thus purely Al_2O_3 with some H impurities. Even though the atom probe is operated under UHV (< 3 × 10⁻¹¹ Torr vacuum), the H signal could be from the residual gas in the chamber. The visible gradient in the Al and O composition is an artifact and related to the electric field which changes during the measurement. Lastly, there is very little O in the bulk.

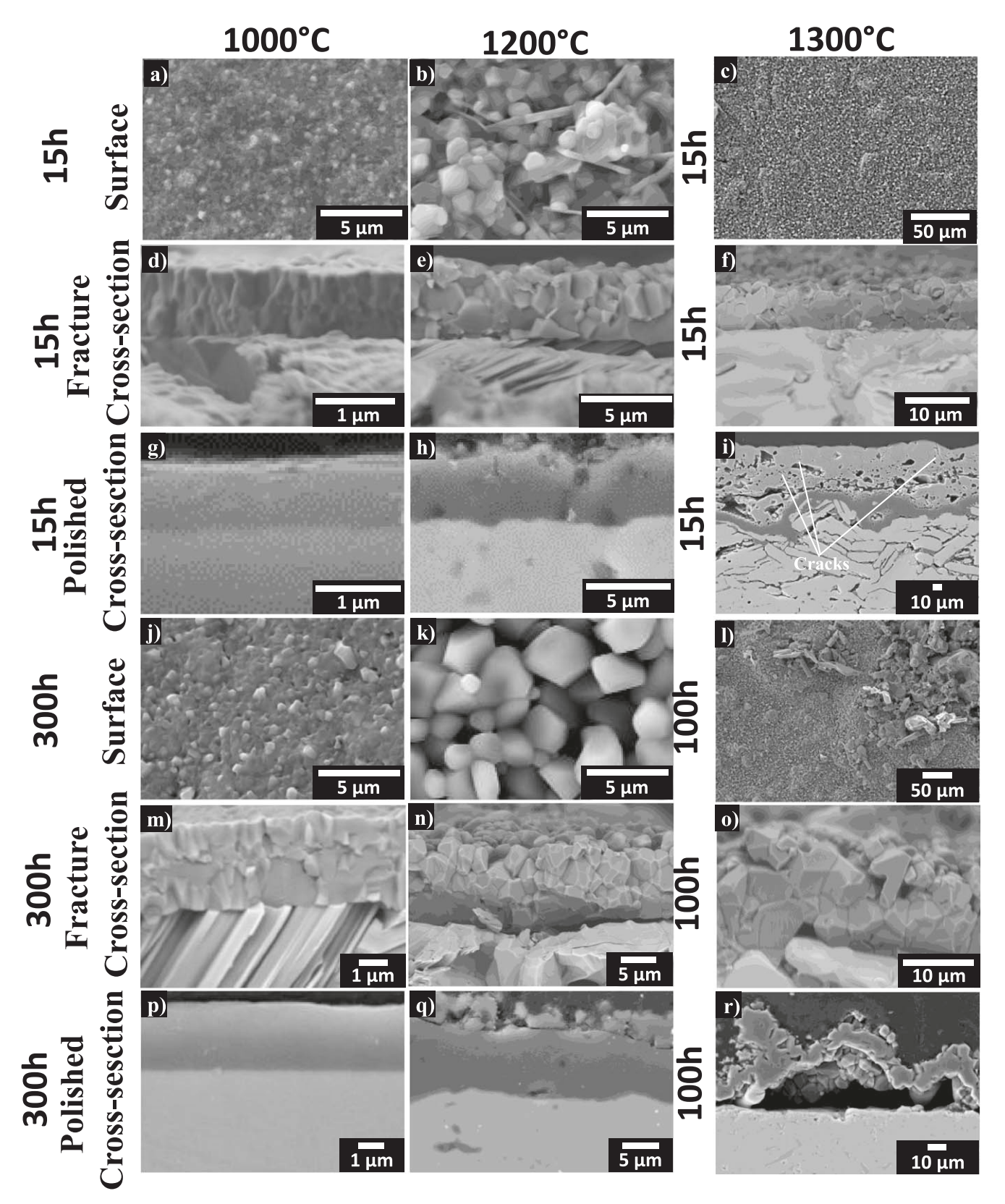


Figure 5. SEM micrographs of oxidized $Ti_3Al_{0.6}Ga_{0.4}C_2$ surface, fracture, and polished cross-section for $Ti_3Al_{0.6}Ga_{0.4}C_2$ after isothermal oxidation in natural air in the 1000 °C-1300 °C range for 15-300 h.

Higher magnification images (Fig. 10) of oxide layers at 1000 °C as a function of time clearly show three regions; outer, inner, and interfacial regions at two magnifications. The left column compares the layers at the same magnification; the right column shows the

same but at higher magnifications (Fig. 10). The inner layer is more columnar than the outer layer which is more equiaxed. The interfacial regions contain grains that are quite small even after 300 h (Fig. 10c). Note that the average width of the grains increases

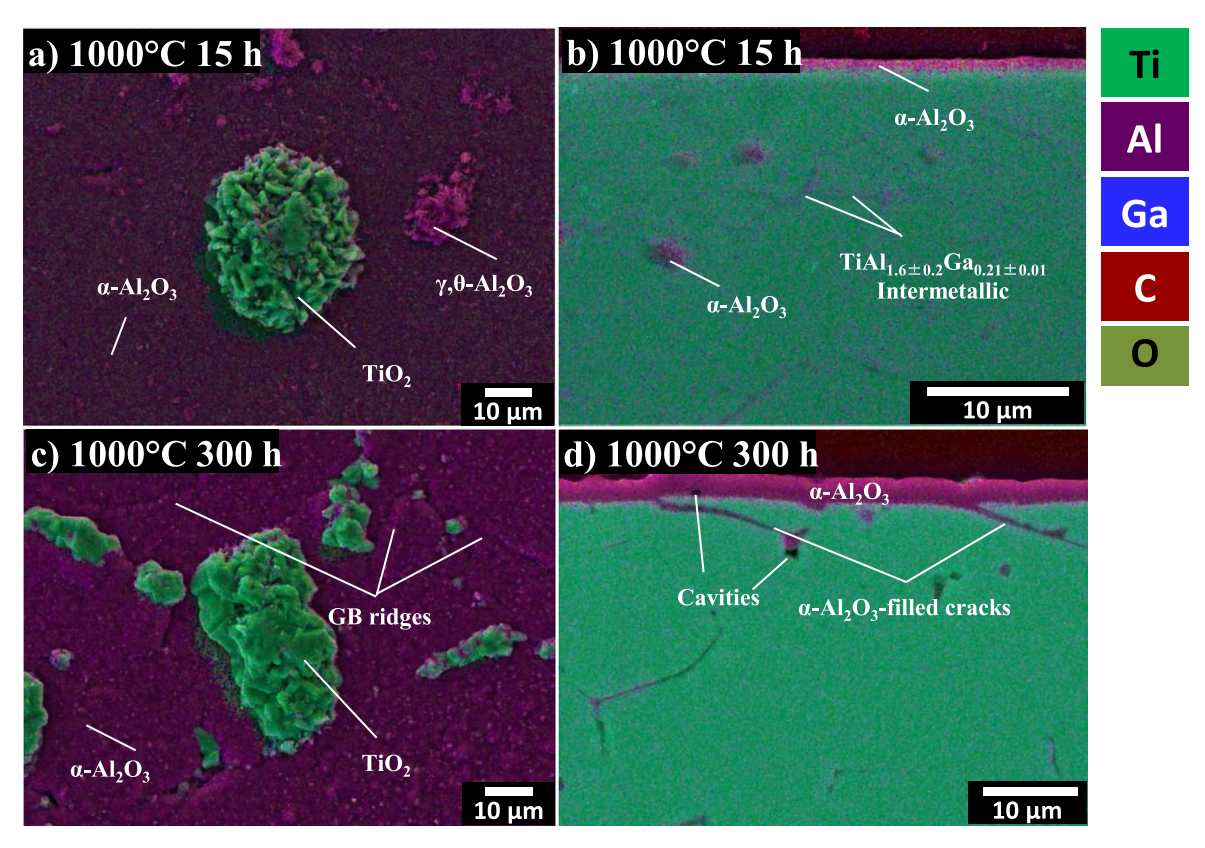


Figure 6. Colorized SEM micrographs after oxidation at 1000 °C. (a) surface EDS map after 15 h, (b) same as a, showing polished, cross-section (c) surface EDS map after 300 h, (d) same as c showing polished, cross-section.

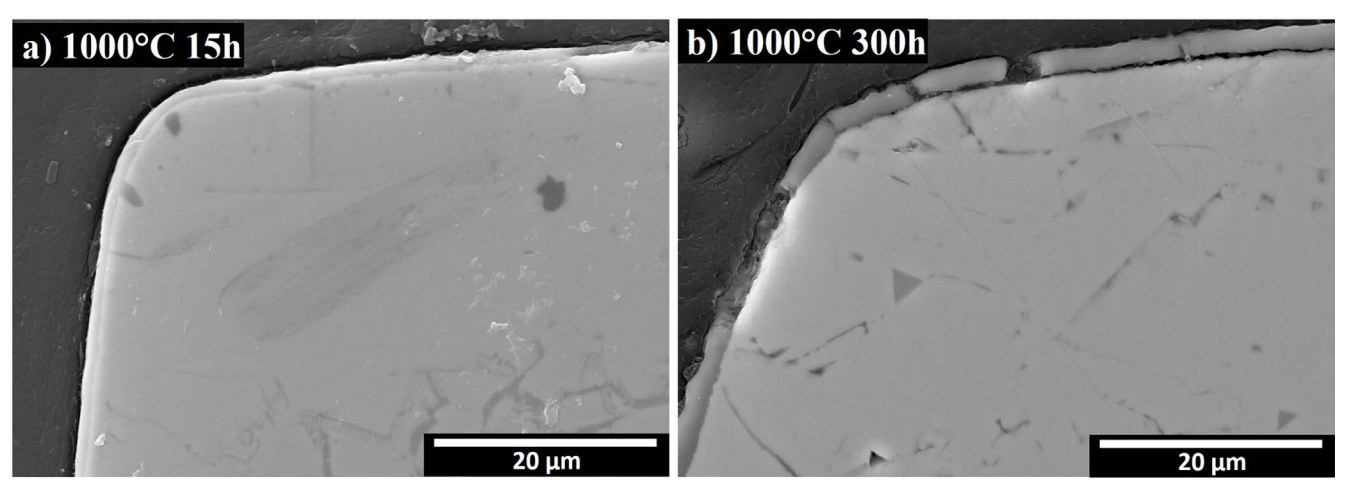


Figure 7. Sample corners after isothermal oxidation 1000 °C for (a) 15 and (b) 300 h. The cracks and delamination most probably occurred during mounting the polishing the sample.

with time (Fig. 10e). More importantly, the ratio of the thicknesses of the outer to inner grains is *not* a function of temperature.

Further, a streak of Al-rich impurity is detected in the substrate as shown in the EDX line profile of Fig. 10d. There is no Ga or O detected through the streak. To the best of our knowledge such streaks have never been observed before in any MAX phase and at this time remain a mystery.

Discussion

Based on the totality of our results it is reasonable to assume that at $T < 1300\,^{\circ}\text{C}$, the oxidation reaction at short times is

$$Ti_{3}Al_{0.6}Ga_{0.4}C_{2} + \left(x + \frac{3y}{4} + z\right)O_{2} \to Ti_{3-x}$$

$$\times Al_{0.6-y}Ga_{0.4}C_{2-z} + xTiO_{2} + \frac{y}{2}Al_{2}O_{3}$$

$$+ zCO_{2}(g)$$
[5]

After the formation of a passivating Al_2O_3 layer, TiO_2 formation stops and the reaction is:

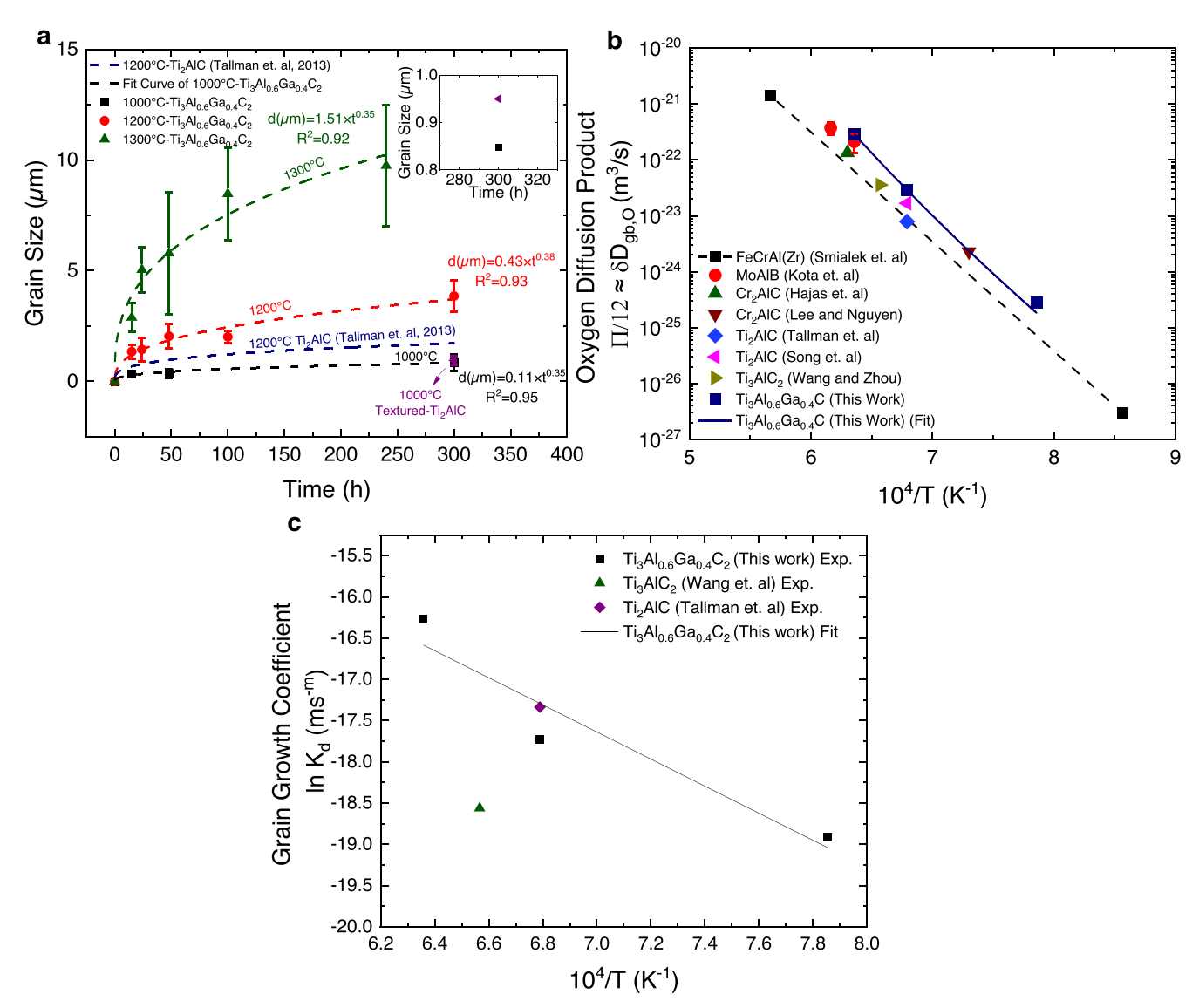


Figure 8. (a) Alumina grain size dependence on oxidation time at $1000 \,^{\circ}\text{C}$ – $1300 \,^{\circ}\text{C}$, respectively, $1200 \,^{\circ}\text{C}$ Ti₂AlC (blue) taken from Ref. 45. Inset compares grain size for solid-solution to ternary textured Ti₂AlC. Grain size at $1000 \,^{\circ}\text{C}$ was estimated from STEM images of individual grains. (b) oxygen diffusion product of Ti₃Al_{0.6}Ga_{0.4}C₂ compared to alumina-forming FeCrAl(Zr) alloy, MoAlB and select MAX phases extracted from Refs. 20,45,47,48,52. (c) Arrhenian-type plot for grain growth kinetics in the $1200 \,^{\circ}\text{C}$ – $1300 \,^{\circ}\text{C}$ range. Data extracted from Refs. 45,53.

$$Ti_{3-x}Al_{0.6-y}Ga_{0.4}C_{2-z} + \left(\frac{3w}{4} + s\right)O_2 \to Ti_{3-x}$$

 $\times Al_{0.6-y-w}Ga_{0.4}C_{2-z-s} + \frac{w}{2}Al_2O_3 + sCO_2$ [6]

At 1300 °C, a ternary oxide is formed according to

$$TiO_2 + Al_2O_3 \rightarrow Al_2TiO_5$$
 [7]

The formation of CO_2 has been shown experimentally elsewhere, it is suspected to be a contributing factor to the observed wrinkling of $\Delta I_0 O_2^{-53}$

The following can also be deduced from our results:

i. At 1000 °C and 1200 °C, $Ti_3Al_{0.6}Ga_{0.4}C_2$ forms a protective adherent α -Al₂O₃ layer. This is quite remarkable since the Al molar ratio in the solid solution is only 10 mol% (\sim 8 wt%). This value is significantly lower than for Ti_xAl_y alloys, where the Al content has to be > 50 at.% for Al₂O₃ to form. ^{56–58} This is important since we have repeatedly shown that for a given

atomic fraction, the activity of Al in the MAX phases is much higher than in most other Ti aluminides. Along the same lines, the end member Ti_3AlC_2 is close to the border of forming Al_2O_3 ; sometimes it forms alumina while other times it does not. ^{59–61} That $\text{Ti}_3\text{Al}_{0.6}\text{Ga}_{0.4}\text{C}_2$ with even less Al, forms a protective Al_2O_3 layer indicates that somehow the presence of Ga in the A-planes may increase the Al activity to the point that a protective Al_2O_3 film forms even at that low concentration.

- No trace of Ga was observed in the scale, even at the interface (Fig. 9). This implies that it either somehow escapes through the Al₂O₃ layer or, more likely, is redistributed into the bulk or GBs.
- At 1200 °C, the Al₂O₃ grain sizes are larger than those reported for Ti₂AlC (Fig. 8a). 45 Why or how, that results in faster oxidation kinetics is unclear at this time.
- iv. Based on the lack of delamination of the oxide at the sample corners after oxidation at 1000 °C for 300 h (Fig. 7) and at 1200 °C for the same time (Fig. S7b) one can conclude that the lateral stresses generated in the oxide scale due to the lateral growth of the Al₂O₃ grains are either small or are relieved by creep. The situation at 1300 °C is quite different since the

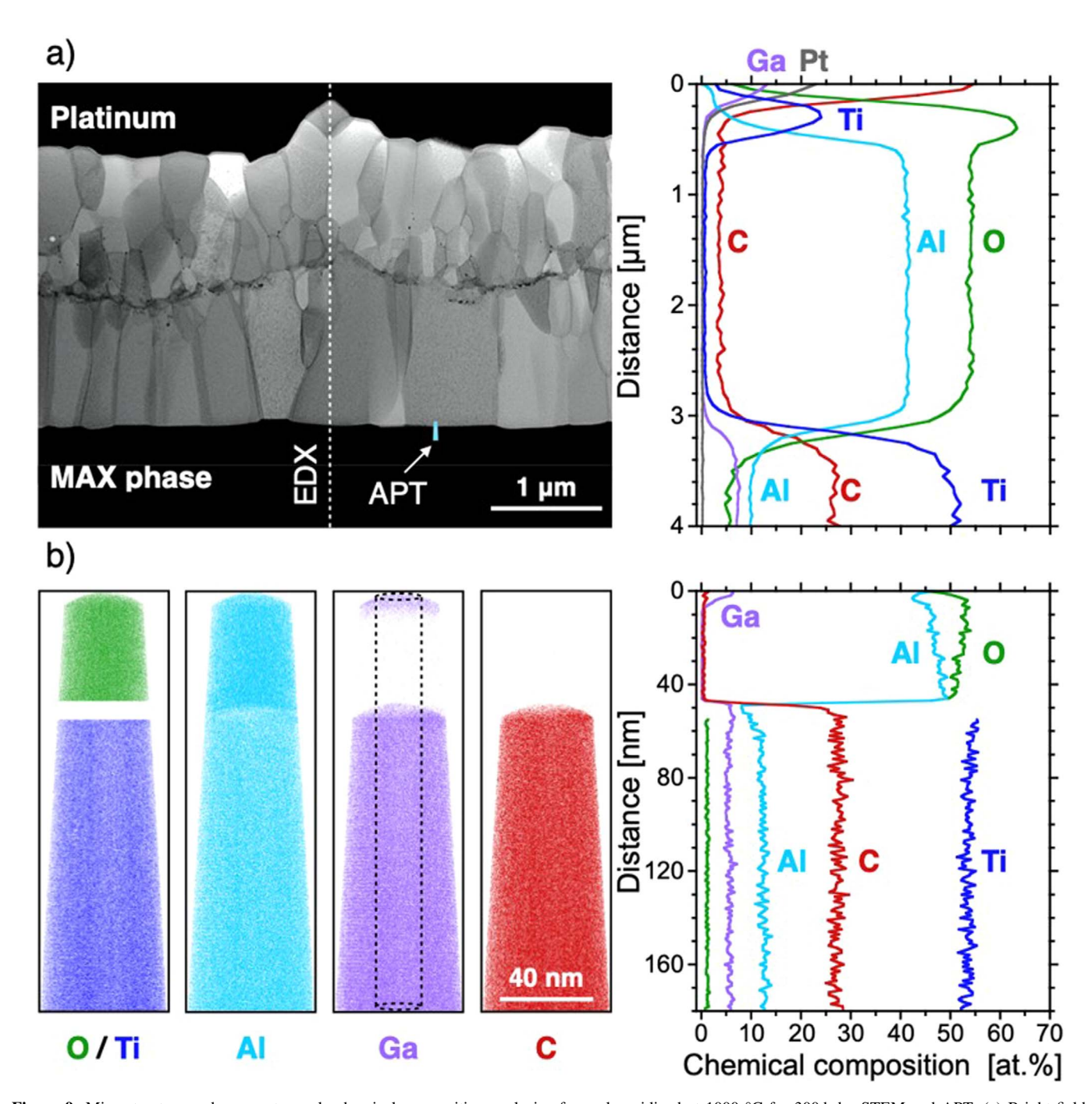


Figure 9. Microstructure and nanometer-scale chemical composition analysis of sample oxidized at 1000 °C for 300 h by STEM and APT. (a) Bright-field micrograph and EDS line scan from the region indicated in the micrograph by a dashed vertical line. (b) Reconstruction of Ti, Al, Ga, C and O atomic positions and chemical composition profile by APT. The extraction region of atom probe specimen is indicated in (a).

oxide scale forms what has been referred to as a "dogbone" structure. 49 In our case, however, the bulk does not deform. The wrinkling observed can be attributed to the lateral growth of the ${\rm Al}_2{\rm O}_3$ grains. 53

The predicted weight gains based on the latter values (Fig. 1c) are less than those measured by 14.4%, 10.8%, and 34.0% at 1000 °C, 1200 °C, and 1300 °C, respectively. There are various reasons that could be contributing to the deviation from predicted and actual weight gains. Primarily due to the internal incorporation of oxygen into the MAX phase. 47,52,61,62 However we only see a small oxygen gradient through the substrate (Fig. 9). Other contributing reasons include topmost oxide particles buried underneath polymer

mounting; excluded localized regions of ${\rm TiO_2}$ and ${\rm Al_2TiO_5}$ both leading to thickness underestimation.

The apparent activation energy for oxidation (191 kJ mol⁻¹), assuming cubic kinetics (Fig. 1d) agrees with Wang and Zhou⁶³ for Ti₃AlC₂ in 1000 °C-1400 °C range (175 kJ mol⁻¹), less than that for Ti₂AlC (250 kJ mol⁻¹) in 1100 °C-1200 °C range, and much lower than Cr₂AlC in 1100 °C-1200 °C range (507 kJ mol⁻¹).⁴⁵

To gain further insight into the controlling mechanism for oxidation, we followed the procedure outlined by Smialek et al. 20 to analyze the underlying mechanism of oxidation. The main highlight of the study is the interfacial grain boundary diffusivity of oxygen through Al_2O_3 in Al_2O_3 -formers follows essentially the same temperature dependence as oxygen diffusion through high-

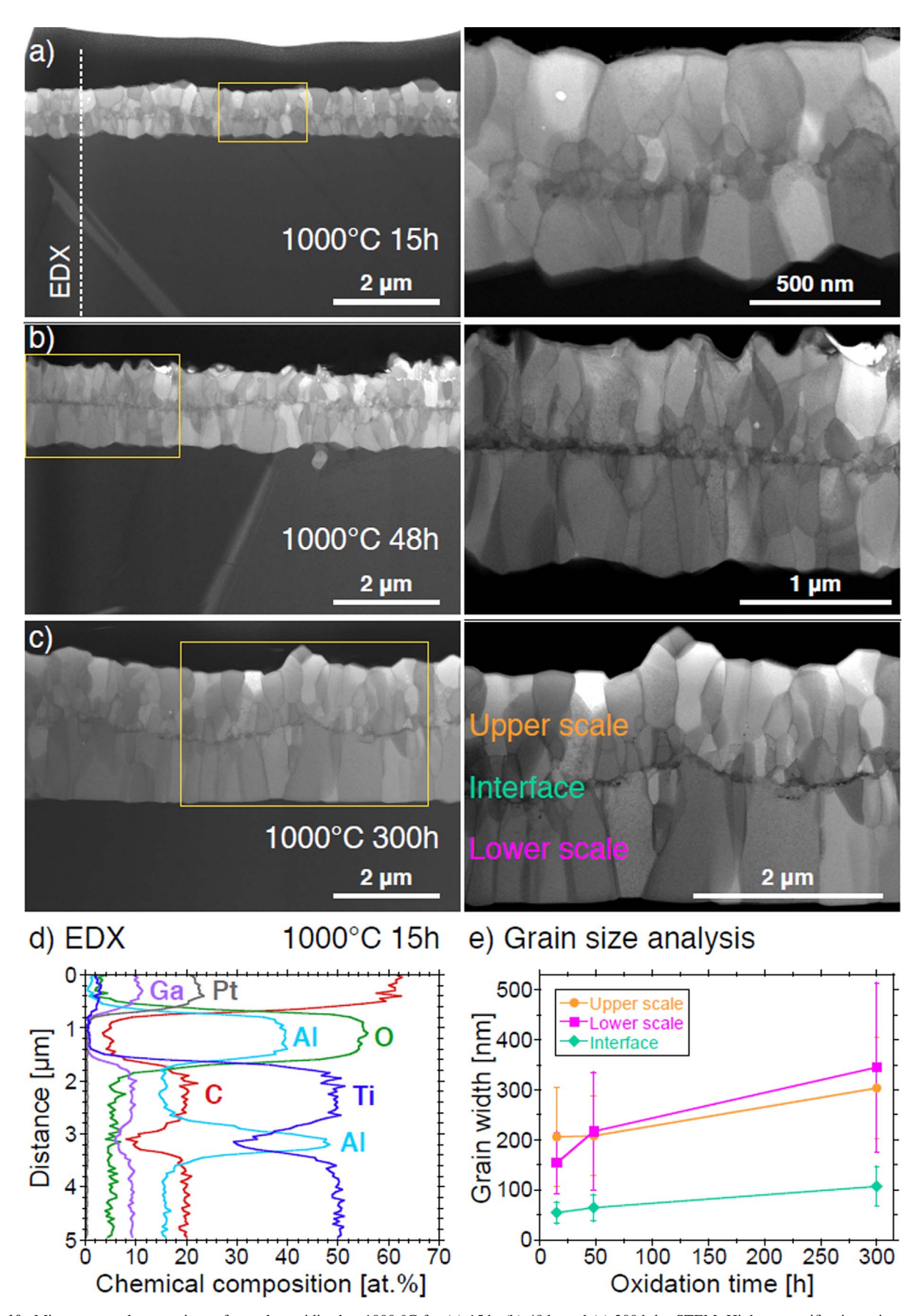


Figure 10. Microstructural comparison of samples oxidized at 1000 °C for (a) 15 h, (b) 48 h, and (c) 300 h by STEM. Higher magnification micrographs are shown in the right panel and the region is indicated by a box in the left panel. (d) EDS linescan from the sample oxidized at 1000 °C for 15 h and the region is indicated in (a). (e) Grain width analysis of the upper and lower oxide scale as well as the interface between the two scales.

purity, bulk poly-crystalline Al_2O_3 . Smialek defines a nearly time-invariant constant Π_i proportional to the interfacial oxygen grain boundary diffusivity, $D_{gb,O,int}$ as

$$\Pi_i = k_{p,i}G_i = 12\delta D_{gh,O,int}$$
 [8]

where δ is the grain boundary width (assumed to be \sim 1 nm), $k_{p,i}$ is the instantaneous parabolic rate constant (see Table III and Ref. 20), and G_i is the instantaneous grain size growth constant (see Eq. 9 and Fig. 8a). Using this approach, we estimate interfacial oxygen diffusion product Π_i at 1000 °C in 1–300 h range to be 2.9×10^{-25} m³s⁻¹ to 2.8×10^{-25} m³s⁻¹ with a median value of 2.8×10^{-25} m³s⁻¹ at 150 h as shown in Fig. 8b. At 1200 °C, in the 1–300 h range, Π_i ranges from 9.7×10^{-24} m³s⁻¹ to 3.4×10^{-23} m³s⁻¹. The median value is 2.9×10^{-23} m³s⁻¹ at 150 h as shown in Fig. 8b. At 1300 °C, in the 1–240 h range, Π_i ranges from 1.5×10^{-22} m³s⁻¹ to 3.1×10^{-22} m³s⁻¹, with a median value of 2.9×10^{-22} m³s⁻¹ at 120 h. When these median values are plotted on an Arrhenian plot (Fig. 8b) they are consistent with other Al₂O₃ forming MAX phases, MoAlB and FeCrAl(Zr) alloys, $^{20.45,51,63,64}$ confirming the common underlying rate controlling mechanism of oxidation, namely the growth of the oxide scale through grain boundary, GB, diffusion.

If the initial grain size, G, is small, the grain growth kinetics can be expressed as: 20

$$G = K_d t^m [9]$$

where K_d is a thermally activated coefficient (Fig. 8c) and m is the grain size exponent. The activation energy for oxide grain growth of ${\rm Ti}_3{\rm Al}_{0.6}{\rm Ga}_{0.4}{\rm C}_2$ is found to be $136 \pm 42\,{\rm kJ~mol}^{-1}$. ${\rm Ti}_2{\rm AlC}$ grain growth exponent is consistent with our findings whereas there is some deviation to that of reported ${\rm Ti}_3{\rm AlC}_2$. The values are comparable indicating similar underlying growth mechanisms. Though the deviation may elucidate some difference in ${\rm Al}_2{\rm O}_3$ grains formed in the MAX solid-solution, compared to those formed on FeCrAl(Zr) (6 wt% or 11 mol% Al nominal content). This difference could be in the form of different solute atoms dissolved in the GBs or in the grains of respective ${\rm Al}_2{\rm O}_3$.

If the kinetics are indeed GB controlled then, μ which is equal 1/m, is related to n in Eq. 3 by:⁶⁶

$$n \approx (\mu - 1)/2\mu$$

At 1000 °C, m is 3.02 and thus n should be 0.35. Coincidentally or not, the experimental n value for oxide thickening is 0.32 ± 0.04 (Table III). This agreement is further evidence that indeed the rate-limiting step is GB diffusion. For reasons that are not clear, the agreement is not as good at 1200 °C.

The nature of diffusing species either Al or O can be deduced by investigation of the multi-layer oxide regions. The equiaxed grain region (Fig. 9a) occupies around 48% of the total oxide thickness. Fig. S8e indicates that the grain width growth is consistent for both top and bottom regions. Figure S8 demonstrates counter current diffusing fluxes of Al and O with inward diffusion of O leading to columnar region. Further, Al and O species meet and nucleate Al₂O₃ at the interface region. This phenomenon was observed in other Al₂O₃ forming compounds such as Cr₂AlC⁶³ and FeCrAl.⁶⁶ It was also shown by 18 O/SIMS that the dual oxide region forms by countercurrent diffusion of Al and O in NiAl and MCrAl alloys.^{67,68}

Mechanistically the micrographs shown in Fig. 10 are significant because if one assumes the inner layer is formed by the inward diffusion of O, with a flux $J_{\rm O}$, and the outer layer by the outward diffusion of Al, with a flux $J_{\rm Al}$, then these results imply that $2\,J_{\rm Al}=3\,J_{\rm O}$. Such dual scales have been observed before and have indeed been explained by the inward diffusion of O through the GBs and the outward diffusion of Al $^{3+}$ through the bulk. $^{68-70}$ The presence of small grains in the interface region even after 300 h (Fig. 10c)

implies that a fraction of the ionic fluxes combines at the interface to form them.

Conclusions

In this work, the isothermal oxidation behavior of bulk hotpressed $T_{i3}Al_{0.6}Ga_{0.4}C_2$ has been investigated, in natural air, from 1000 °C to 1300 °C, for durations up to 300 h. The solid solution exhibited a good oxidation resistance at 1000 °C, with slow, cubic oxidation kinetics due to the formation of a dense, adherent Al_2O_3 protective layer. At 1000 °C, the low weight gain observed indicates that the oxidation resistance of $T_{i3}Al_{0.6}Ga_{0.4}C_2$ is slightly better than those previously reported for both $T_{i3}AlC_2$ and $T_{i2}AlC$. The ratelimiting step in the oxidation is grain boundary diffusion of Al and/ or O through the Al_2O_3 protective layer.

At 1200 °C, with time, the wrinkling of the Al_2O_3 layer results in poor oxidation protection.

At 1300 °C, contrary to the lower temperatures, the weight gain due to oxidation is considerably larger and faster than the values reported for Ti₃AlC₂ and Ti₂AlC. SEM characterization revealed that the oxidized samples were highly inhomogeneous, with some localized but extended regions of TiO₂, likely responsible for the big mass intake observed at this temperature. In addition, in these regions, TiO₂ and Al₂O₃ react to form the ternary Al₂TiO₅ oxide. Even in the areas of the samples where TiO₂ was not observed, the Al₂O₃ was wrinkled and sometimes delaminated. At around 8 at. %, the Al concentration is one of the lowest, if not the lowest, in Tibased alloys/compounds that still form an Al₂O₃ passivating layer.

In conclusion, the maximum use temperature of this solid solution is about 1000 °C. Interestingly, at 1200 °C and 1300 °C, the presence of Ga enhances the grain size of the ${\rm Al_2O_3}$ layer. Why that does not lead to better oxidation resistance is not entirely clear at this time. These comments notwithstanding, Ga seems a promising dopant for Al-based MAX phases and can probably be used to tune other properties of interest, such as creep, which we are currently exploring.

Acknowledgments

The research was supported by National Science Foundation (1729335).

ORCID

Tarek A. ElMeligy https://orcid.org/0000-0002-5033-6317 Maxim Sokol https://orcid.org/0000-0001-8588-0585

References

- W. G. Fahrenholtz and G. E. Hilmas, "Ultra-high temperature ceramics: Materials for extreme environments." Scr. Mater., 129, 94 (2017).
- J. T. A. Roberts and J. T. A. Roberts, Steam Turbine Materials, in: Struct. Mater. Nucl. Power Syst. (Springer, Berlin) p. 405 (1981).
- J. T. A. Roberts, Structural Materials in Nuclear Power Systems (Springer, Berlin) (1981).
- T. M. Pollock and S. Tin, "Nickel-based superalloys for advanced turbine engines: Chemistry, microstructure, and properties." J. Propuls. Power., 22, 361 (2006).
- T. Yano and B. Matović, "Advanced ceramics for nuclear applications." *Handb. Adv. Ceram. Mater. Appl. Process. Prop.* (Elsevier, USA) p. 353 (2013), in.
 M. Barsoum and T. El-Raghy, "The MAX phases: unique new carbide and nitride
- M. Barsoum and T. El-Raghy, "The MAX phases: unique new carbide and nitride materials: ternary ceramics turn out to be surprisingly soft and machinable, yet also heat-tolerant, strong." Am. Sci., 89, 334 (2001).
- M. W. Barsoum and M. Radovic, "Elastic and mechanical properties of the MAX phases." Annu. Rev. Mater. Res., 41, 195 (2011).
- M. Sokol, V. Natu, S. Kota, and M. W. Barsoum, "On the chemical diversity of the MAX phases." *Trends Chem.*, 1, 210 (2019).
- 9. M. W. Barsoum, MAX Phases: Properties Of Machinable Ternary Carbides And Nitrides (Wiley, Weinheim, Germany) (2013).
- J. L. Smialek, "Oxidation of Al₂O₃ scale-forming MAX phases in turbine environments." Metall. Mater. Trans. A Phys. Metall. Mater. Sci., 49, 782 (2018).
- 11. M. Sundberg, G. Malmqvist, A. Magnusson, and T. El-Raghy, "Alumina forming high temperature silicides and carbides." *Ceram. Int.*, **30**, 1899 (2004).
- M. Sokol, J. Yang, H. Keshavan, and M. W. Barsoum, "Bonding and oxidation protection of Ti₂AlC and Cr₂AlC for a Ni-based superalloy." *J. Eur. Ceram. Soc.*, 39, 878 (2019).

- B. A. Pint, K. A. Terrani, Y. Yamamoto, and L. L. Snead, "Material selection for accident tolerant fuel cladding," *Metall. Mater. Trans. E.*, 2, 190 (2015).
- Q. M. Wang, W. Garkas, A. F. Renteria, C. Leyens, and K. H. Kim, "Oxidation behaviour of Ti₂AlN films composed mainly of nanolaminated MAX phase." *J. Nanosci. Nanotechnol.*, 11, 8959 (2011).
- S. Gupta, D. Filimonov, and M. W. Barsoum, "Isothermal oxidation of Ta₂AlC in air." J. Am. Ceram. Soc., 89, 2974 (2006).
- J. Gonzalez-Julian, S. Onrubia, M. Bram, C. Broeckmann, R. Vassen, and O. Guillon, "High-temperature oxidation and compressive strength of Cr₂AlC MAX phase foams with controlled porosity." *J. Am. Ceram. Soc.*, 101, 542 (2018).
- J. Gonzalez-Julian, T. Go, D. E. Mack, and R. Vaßen, "Environmental resistance of Cr₂AlC MAX phase under thermal gradient loading using a burner rig." *J. Am. Ceram. Soc.*, 101, 1841 (2018).
- J. Gonzalez-Julian, G. Mauer, D. Sebold, D. E. Mack, and R. Vassen, "MAX phase as bond coat for thermal barrier coatings: processing, testing under thermal gradient loading, and future challenges." J. Am. Ceram. Soc., 103, 2362 (2020).
- J. L. Smialek, J. A. Nesbitt, T. P. Gabb, A. Garg, and R. A. Miller, "Hot corrosion and low cycle fatigue of a Cr₂AlC-coated superalloy." *Mater. Sci. Eng. A*, 711, 119 (2018).
- J. L. Smialek, "Oxygen diffusivity in alumina scales grown on Al-MAX phases." Corros. Sci., 91, 281 (2015).
- J. L. Smialek and A. Garg, "Interfacial reactions of a MAX phase/superalloy hybrid." Surf. Interface Anal., 47, 844 (2015).
- J. L. Smialek, "Kinetic aspects of Ti₂AIC MAX phase oxidation." Oxid. Met., 83, 351 (2015).
- J. L. Smialek, B. J. Harder, and A. Garg, "Oxidative durability of TBCs on Ti₂AlC MAX phase substrates." Surf. Coatings Technol., 285, 77 (2016).
- S. Basu, N. Obando, A. Gowdy, I. Karaman, and M. Radovic, "Long-term oxidation of Ti₂AlC in air and water vapor at 1000 °C-1300 °C temperature range." *J. Electrochem. Soc.*, 159, C90 (2012).
- D. Horlait, S. Grasso, N. Al Nasiri, P. A. Burr, and W. E. Lee, "Synthesis and oxidation testing of MAX phase composites in the Cr-Ti-Al-C quaternary system." *J. Am. Ceram. Soc.*, 99, 682 (2016).
- G. Bei, B. J. Pedimonte, T. Fey, and P. Greil, "Oxidation behavior of MAX phase Ti₂Al_(1-x)Sn_xC solid solution." J. Am. Ceram. Soc., 96, 1359 (2013).
- J. W. Byeon, J. Liu, M. Hopkins, W. Fischer, N. Garimella, K. B. Park, M. P. Brady, M. Radovic, T. El-Raghy, and Y. H. Sohn, "Microstructure and residual stress of alumina scale formed on Ti₂AlC at high temperature in air." Oxid. Met., 68, 97 (2007).
- M. Sundberg, G. Malmqvist, A. Magnusson, and T. El-Raghy, "Alumina forming high temperature silicides and carbides." (2004), in Ceram. Int., pp 1899.
- H. Gao, R. Benitez, W. Son, R. Arroyave, and M. Radovic, "Structural, physical and mechanical properties of Ti₃(Al_{1-x}Si_x)C₂ solid solution with x = 0-1." *Mater. Sci. Eng. A*, 676, 197 (2016).
- M. Radovic, M. W. Barsoum, A. Ganguly, T. Zhen, P. Finkel, S. R. Kalidindi, E. Lara-Curzio, E. Laracurzio, and E. Lara-Curzio, "On the elastic properties and mechanical damping of Ti₃SiC₂, Ti₃GeC₂, Ti₃Si_{0.5}Al_{0.5}C₂ and Ti₂AlC in the 300-1573 K temperature range." *Acta Mater.*, 54, 2757 (2006).
- 31. J. C. Lee, S. W. Park, and D. B. Lee, "Oxidation of Ti₃Al_{0.3}Si_{0.7}C₂ compounds at 900 °C-1200 °C in air." *Curr. Nanosci.*, **10**, 97 (2014).
- G. P. Bei, V. Gauthier-Brunet, C. Tromas, and S. Dubois, "Synthesis, characterization, and intrinsic hardness of layered nanolaminate Ti₃AlC₂ and Ti₃Al_{0.8}Sn_{0.2}C₂ solid solution." *J. Am. Ceram. Soc.*, 95, 102 (2012).
- Z. Huang, H. Xu, H. Zhai, Y. Wang, and Y. Zhou, "Strengthening and tribological surface self-adaptability of Ti₃AlC₂ by incorporation of Sn to form Ti₃Al(Sn)C₂ solid solutions." *Ceram. Int.*, 41, 3701 (2015).
- W. Yu, V. Gauthier-Brunet, T. Cabioc'H, and S. Dubois, "Synthesis and microstructural characterization of substoichiometric Ti₂Al(C_xN_y) solid solutions and related Ti₂AlC_x and Ti₂AlN end-members." *J. Am. Ceram. Soc.*, 97, 2308 (2014).
 M. W. Barsoum, M. Ali, and T. El-Raghy, "Processing and characterization of
- M. W. Barsoum, M. Ali, and T. El-Raghy, "Processing and characterization of Ti₂AlC, Ti₂AlN, and Ti₂AlC_{0.5}N_{0.5}." *Metall. Mater. Trans. A Phys. Metall. Mater.* Sci., 31, 1857 (2000).
- W. Yu, S. Li, and W. G. Sloof, "Microstructure and mechanical properties of a Cr₂Al(Si)C solid solution." *Mater. Sci. Eng. A*, 527, 5997 (2010).
- M. W. Barsoum, I. Salama, T. El-Raghy, J. Golczewski, W. D. Porter, H. Wang, H. J. Seifert, and F. Aldinger, "Thermal and electrical properties of Nb₂AlC, (Ti,Nb)₂AlC and Ti₂AlC." *Metall. Mater. Trans. A Phys. Metall. Mater. Sci.*, 33, 2775 (2002).
- I. Salama, T. El-Raghy, and M. W. Barsoum, "Synthesis and mechanical properties of Nb₂AlC and (Ti,Nb)₂AlC." J. Alloys Compd., 347, 271 (2002).
- V. G. Hill, R. Roy, and E. F. Osborn, "The System Alumina-Gallia-Water." J. Am. Ceram. Soc., 35, 135 (1952).
- M. Shamma, E. N. Caspi, B. Anasori, B. Clausen, D. W. Brown, S. C. Vogel, V. Presser, S. Amini, O. Yeheskel, and M. W. Barsoum, "In situ neutron diffraction evidence for fully reversible dislocation motion in highly textured polycrystalline Ti₂AlC samples." *Acta Mater.*, 98, 51 (2015).

- J. Rodríguez-Carvajal, "Recent advances in magnetic structure determination by neutron powder diffraction." Phys. B Phys. Condens. Matter., 192, 55 (1993).
- K. Thompson, D. Lawrence, D. J. Larson, J. D. Olson, T. F. Kelly, and B. Gorman, "In situ site-specific specimen preparation for atom probe tomography." *Ultramicroscopy*, 107, 131 (2007).
- H. M. Rietveld, "A profile refinement method for nuclear and magnetic structures."
 J. Appl. Crystallogr., 2, 65 (1969).
- X. H. Wang and Y. C. Zhou, "High-temperature oxidation behavior of Ti₂AlC in air." Oxid. Met., 59, 303 (2003).
- D. J. Tallman, B. Anasori, and M. W. Barsoum, "A critical review of the oxidation of Ti₂AlC, Ti₃AlC₂ and Cr₂AlC in Air." *Mater. Res. Lett.*, 1, 115 (2013).
- Z. J. Lin, M. S. Li, J. Y. Wang, and Y. C. Zhou, "High-temperature oxidation and hot corrosion of Cr₂AlC." *Acta Mater.*, 55, 6182 (2007).
- M. Dahlqvist, B. Alling, I. A. Abrikosov, and J. Rosén, "Phase stability of Ti₂AlC upon oxygen incorporation: A first-principles investigation." *Phys. Rev. B*, 81 (2010).
- 48. B. Pieraggi, "Calculations of parabolic reaction rate constants." Oxid. Met., 27, 177 (1987)
- F. A. Golightly, F. H. Stott, and G. C. Wood, "The influence of yttrium additions on the oxide-scale adhesion to an iron-chromium-aluminum alloy." *Oxid. Met.*, 10, 163 (1976).
- D. Naumenko, B. Gleeson, E. Wessel, L. Singheiser, and W. J. Quadakkers, "Correlation between the microstructure, growth mechanism, and growth kinetics of alumina scales on a FeCrAIY alloy." *Metall. Mater. Trans. A*, 38, 2974 (2007).
- S. Kota, E. Zapata-Solvas, Y. Chen, M. Radovic, W. E. Lee, and M. W. Barsoum, "Isothermal and Cyclic Oxidation of MoAlB in Air from 1100 °C to 1400 °C." *J. Electrochem. Soc.*, 164, C930 (2017).
- P. O. Persson, J. Rosén, D. R. McKenzie, and M. M. M. Bilek, "Formation of the MAX -phase oxycarbide Ti₂AlC_{1-x}O_x studied via electron energy-loss spectroscopy and first-principles calculations." *Phys. Rev. B - Condens. Matter Mater. Phys.*, 80, 092102 (2009).
- X. H. Wang, F. Z. Li, J. X. Chen, and Y. C. Zhou, "Insights into high temperature oxidation of Al₂O₃-forming Ti₀AlC₂." *Corros. Sci.*, 58, 95 (2012).
- J. L. Smialek, N. S. Jacobson, B. Gleeson, D. B. Hovis, and A. H. Heuer, "Oxygen permeability and grain-boundary diffusion applied to alumina scales, national aeronautics and space administration." *Glenn Research Center* (2013).
- M. Hans and J. M. Schneider, "Electric field strength-dependent accuracy of TiAlN thin film composition measurements by laser-assisted atom probe tomography." New J. Phys., 22, 033036 (2020).
- R. G. Reddy, X. Wen, and M. Divakar, "Isothermal oxidation of TiAl alloy." Metall. Mater. Trans. A Phys. Metall. Mater. Sci., 32, 2357 (2001).
- S. Becker, A. Rahmel, M. Schorr, and M. Schütze, "Mechanism of isothermal oxidation of the intel-metallic TiAl and of TiAl alloys." Oxid. Met., 38, 425 (1992).
- K. L. Luthra, "Stability of protective oxide films on Ti-base alloys." Oxid. Met., 36475 (1991).
- 59. M. W. Barsoum, N. Tzenov, A. Procopio, T. El-Raghy, and M. Ali, "Oxidation of $Ti_{n+1}AlX_n$ (n=1-3 and X=C,N): II. experimental results." *J. Electrochem. Soc.*, **148**, C551 (2001).
- 60. M. W. Barsoum, "Oxidation of $Ti_{n+1}AlX_n$ (n = 1-3 and X = C, N)." J. Electrochem. Soc., 148, C544 (2001).
- D. B. Lee and S. W. Park, "High-temperature oxidation of Ti₃AlC₂ between 1173 and 1473K in air." *Mater. Sci. Eng. A*, 434, 147 (2006).
- J. Rosen, P. O. Å. Persson, M. Ionescu, A. Kondyurin, D. R. McKenzie, and M. M. M. Bilek, "Oxygen incorporation in Ti₂AlC thin films." *Appl. Phys. Lett.*, 92, 064102 (2008).
- X. H. Wang and Y. C. Zhou, "Oxidation behavior of Ti₃AlC₂ at 1000 °C-1400 °C in air." Corros. Sci., 45, 891 (2003).
- D. E. Hajas, M. To. Baben, B. Hallstedt, R. Iskandar, J. Mayer, and J. M. Schneider, "Oxidation of Cr₂AlC coatings in the temperature range of 1230 °C to 1410 °C, Surf." *Coatings Technol.*, 206, 591 (2011).
- W. Fei, S. C. Kuiry, and S. Seal, "Inhibition of metastable alumina formation on Fe-Cr-Al-Y alloy fibers at high temperature using titania coating." Oxid. Met., 62, 29-44 (2004).
- Z. Liu, W. Gao, and Y. He, "Modeling of oxidation kinetics of Y-doped Fe-Cr-Al alloys." Oxid. Met., 53, 341 (2000).
- A. Farle, L. Boatemaa, L. Shen, S. Gövert, J. B. W. Kok, M. Bosch, S. Yoshioka, S. Van Der Zwaag, and W. G. Sloof, "Demonstrating the self-healing behaviour of some selected ceramics under combustion chamber conditions." *Smart Mater. Struct.*, 25, 084019 (2016).
- W. J. Quadakkers, H. Holzbrecher, K. G. Briefs, and H. Beske, "Differences in growth mechanisms of oxide scales formed on ODS and conventional wrought alloys." Oxid. Met., 32, 67 (1989).
- R. Prescott, D. F. Mitchell, G. I. Sproule, and M. J. Graham, "Transport in α-Al₂O₃ scales on FeAl and NiAl alloys at 1100 °C." Solid State Ionics., 56, 229 (1992).
- B. A. Pint, J. R. Martin, and L. W. Hobbs, "18O/SIMS characterization of the growth mechanism of doped and undoped α-Al₂O₃." Oxid. Met., 39, 167 (1993).

Supplementary Information for: Isothermal Oxidation of $Ti_3Al_{0.6}Ga_{0.4}C_2$ MAX Phase Solid Solution in Air at 1000 to 1300 °C

Tarek A. ElMeligy¹, Enrica Epifano^{2,3}, Maxim Sokol^{1,4}, Gilles Hug², Marcus Hans⁵, Jochen M. Schneider⁵, Michel W. Barsoum ^{1,z}

¹ Drexel University, Department of Materials Science & Engineering, Philadelphia, PA, USA

² Laboratoire d'Etudes des Microstructures, CNRS-ONERA, Boite Postale 72, 92322 Châtillon Cedex, France

³ CIRIMAT laboratory, University of Toulouse, CNRS, INPT, UPS, ENSIACET 4 allée Emile Monso, BP-44362, 31030 Toulouse Cedex 4, France

⁴ Department of Materials Science and Engineering, Tel Aviv University, Ramat Aviv 6997801, Israel

⁵ Materials Chemistry, RWTH Aachen University, Aachen, Germany.

^z Corresponding author.

Table S1: Weight gain kinetic parameters and correlation coefficients derived by fitting oxidation experimental results (Fig. 1a) derived by procedure of $\Delta m \ vs \ t^{1/2}$ plots [1].

	Parabolic					
T (°C)	$k_{p,w} (kg^2m^{-4}s^{-1})$	\mathbb{R}^2				
1300	$2.53 \pm 0.01 \times 10^{-9}$	0.9988				
1200	$2.66 \pm 0.01 \times 10^{-10}$	0.9960				
1000	$2.99 \pm 0.003 \times 10^{-11}$	0.9998				

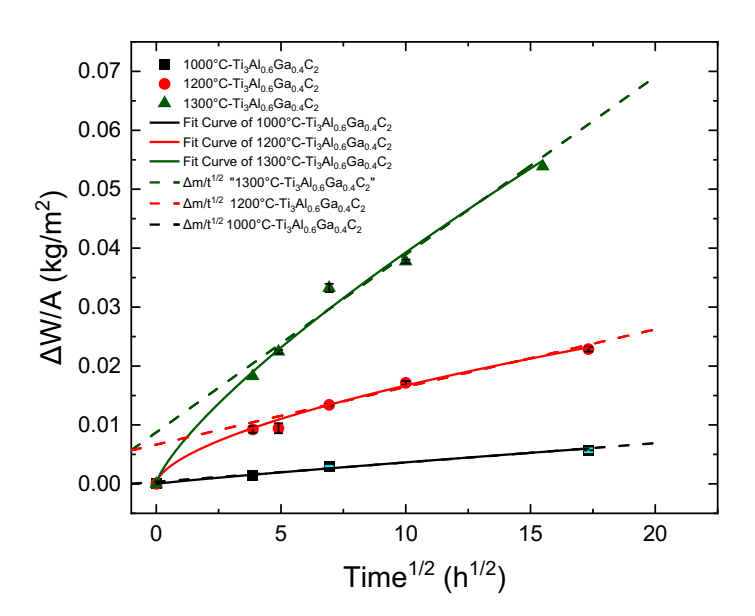


Fig. S1: Temperature dependence of weight gain per unit surface area versus square root of time.

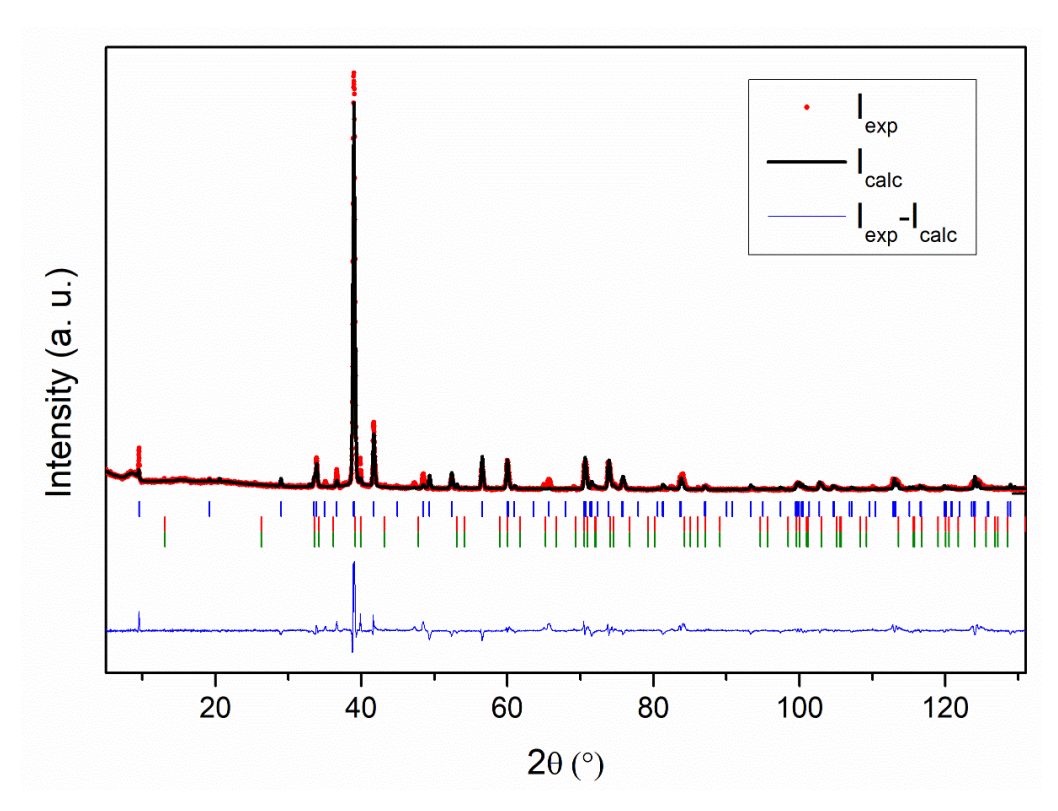


Fig. S2: Powder XRD pattern of $Ti_3Al_{0.6}Ga_{0.4}C_2$ sample. Experimental points are in red, Rietveld-calculated in black, and the difference between them in lower blue line. Ticks below the pattern represent the peak positions of Ti_3AlC_2 (blue ticks), Ti_2AlC (red and green ticks).

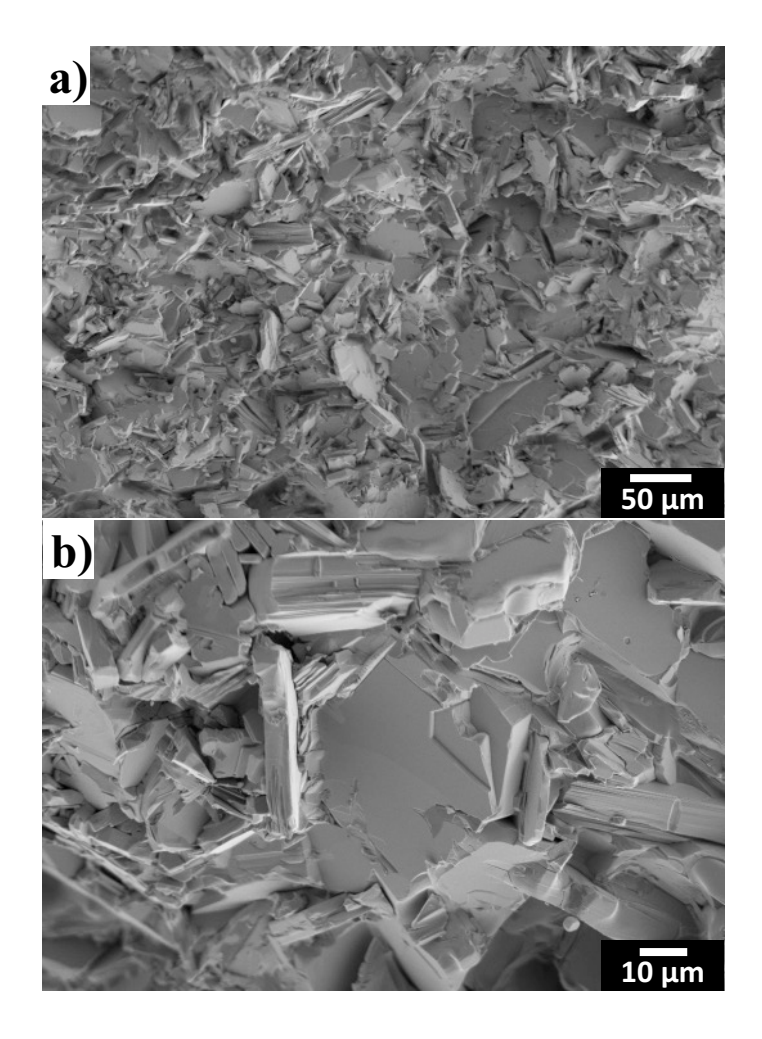


Fig. S3: SEM micrographs of $Ti_3Al_{0.6}Ga_{0.4}C_2$ fracture surface. a) low mag b) high mag of nanolaminated structure.

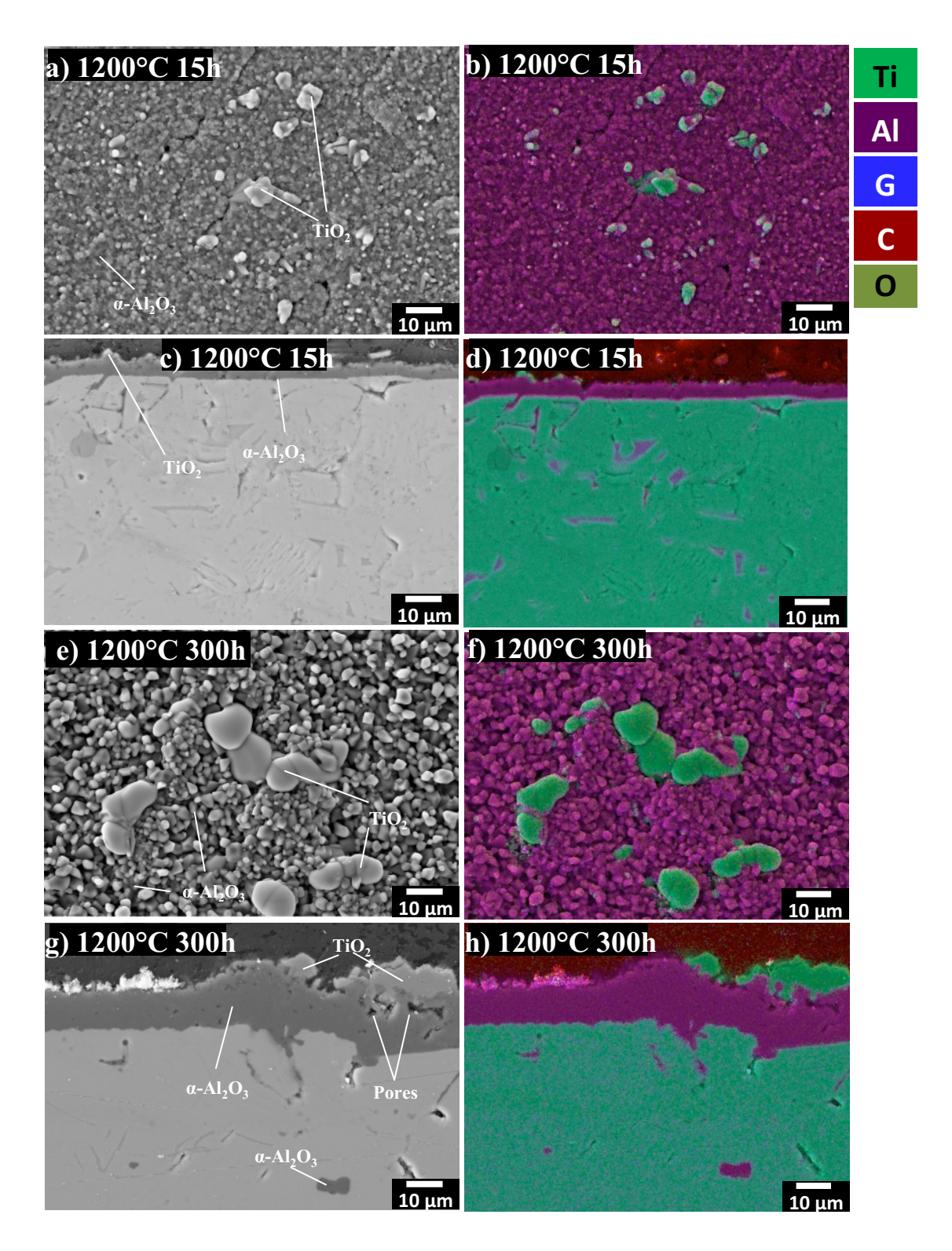


Fig. S4: Colorized SEM micrographs after oxidation at 1200°C. a) surface SE image after 15 h, b) same as a showing EDS map, c) polished cross-section SE image after 15 h, d) same as c showing EDS map, e) surface SE image after 300 h, f) same as e showing EDS map, g) polished cross-section SE image after 300h, h) same as g showing EDS map

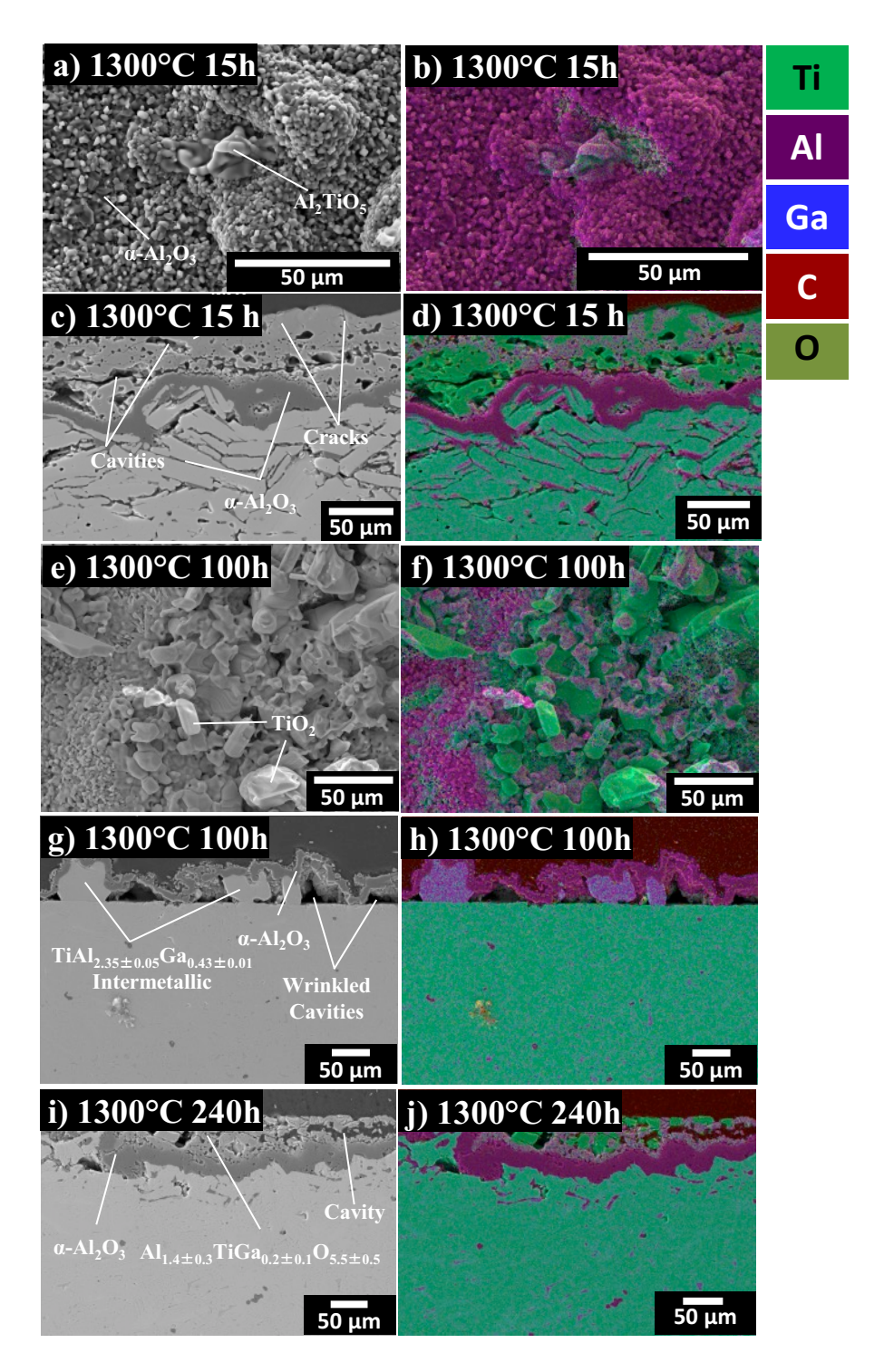


Fig. S5: Colorized SEM micrographs after oxidation at 1300°C. a) surface SE image after 15 h, b) same as a showing EDS map, c) polished cross-section SE image after 15h, d) same as c showing EDS map, e) surface SE image after 300h, f) same as e showing EDS map, g) polished cross-section SE image after 300 h, h) same as g showing EDS map.

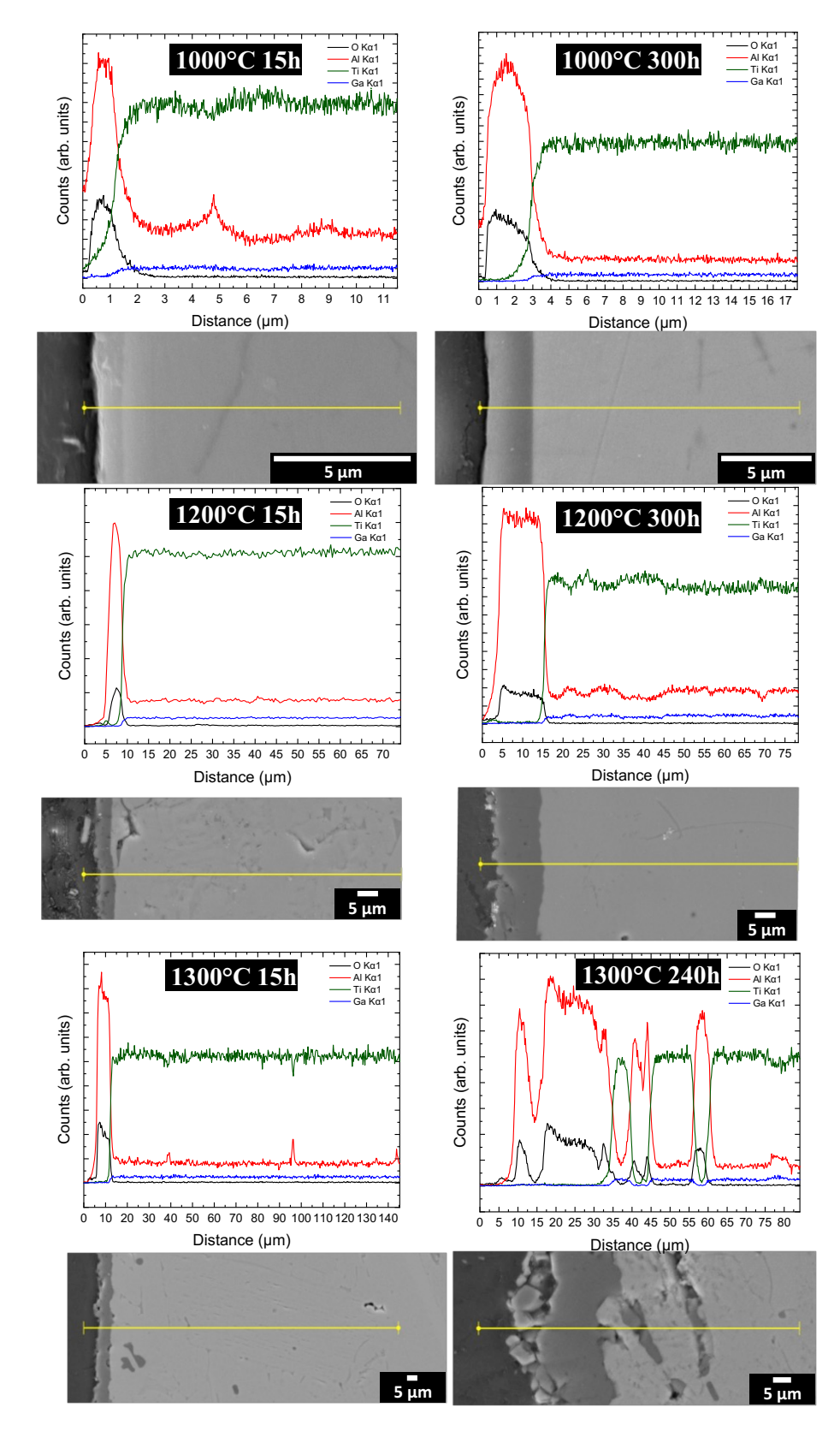


Fig. S6: EDS line scan profiles across the MAX/oxide interface at $1000\text{-}1300^{\circ}\text{C}$ after 15-300 h showing relative concentrations of O, Al, Ti and Ga.

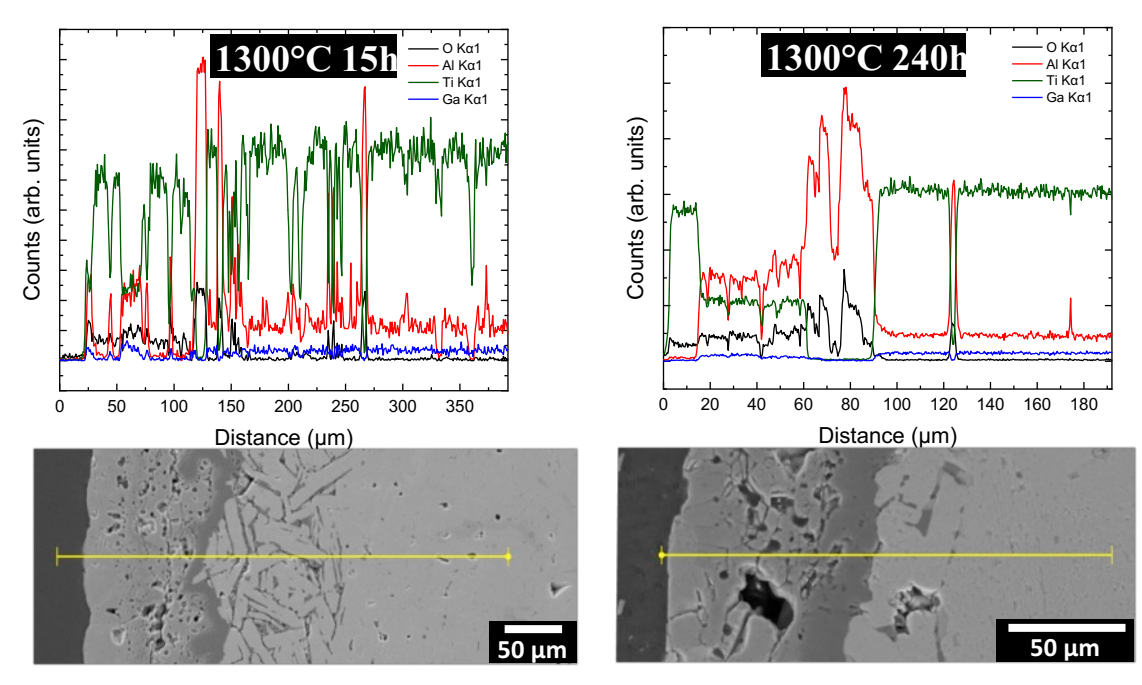


Fig. S7: EDS line scan profiles across the MAX/oxide interface at 1300° C after 15-240h for TiO_2 rich islands showing relative concentrations of O, Al, Ti and Ga.

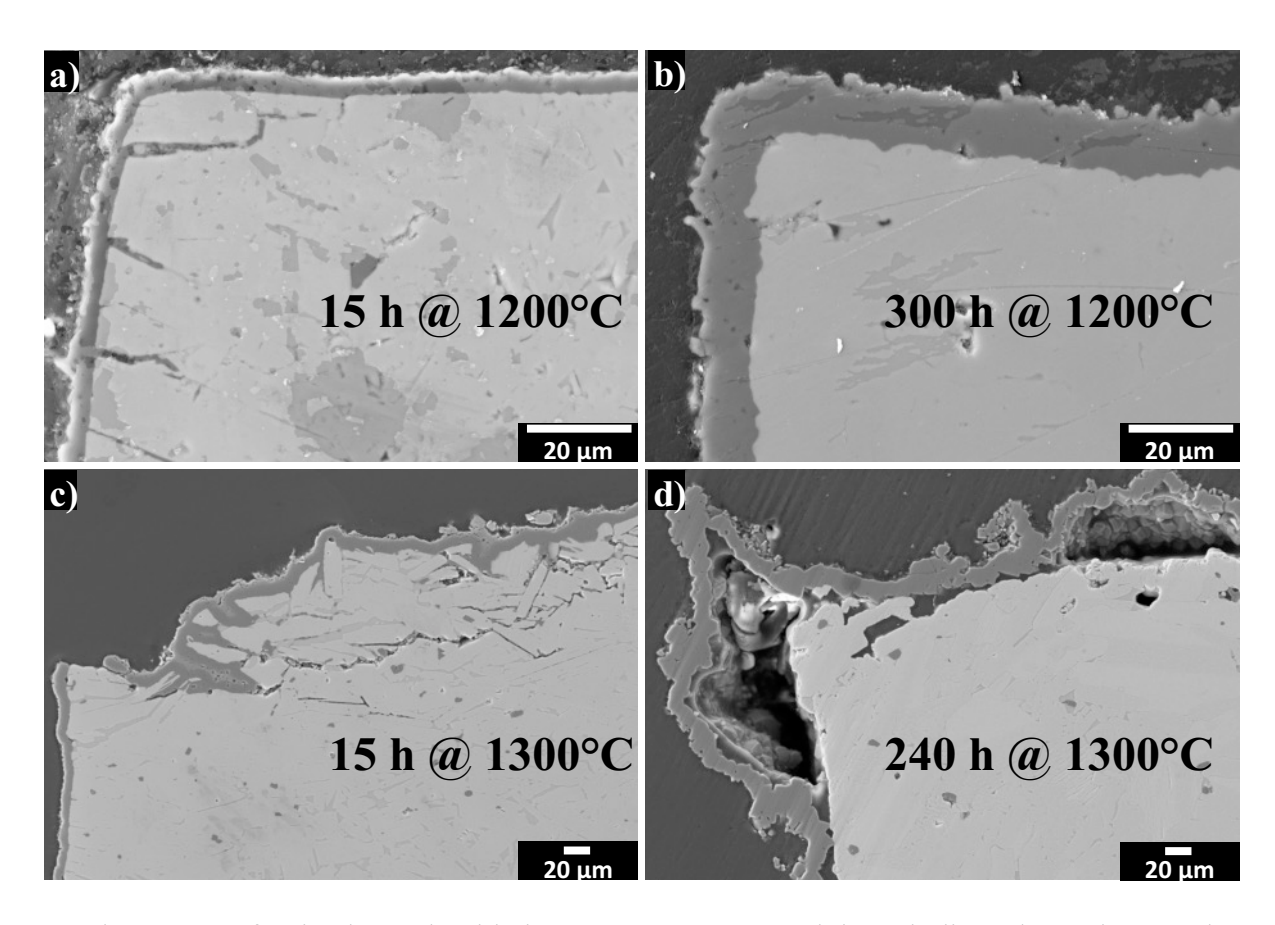


Fig. S8: Sample corners after isothermal oxidation at temperatures and times indicated on micrographs.

References

[1] B. Pieraggi, Calculations of parabolic reaction rate constants, Oxid. Met. 27 (1987) 177–185.